

Report on Progress

Nanoscale electrodynamics of strongly correlated quantum materials

Mengkun Liu¹, Aaron J Sternbach^{2,3} and D N Basov^{2,3}

¹ Department of Physics, Stony Brook University, Stony Brook, NY 11794, USA

² Department of Physics, University of California, San Diego, La Jolla, CA 92093, USA

³ Department of Physics, Columbia University, New York, NY 10027, USA

E-mail: mengkun.liu@stonybrook.edu and dbasov@physics.ucsd.edu

Received 23 December 2015, revised 23 May 2016

Accepted for publication 2 June 2016

Published 3 November 2016



Corresponding editor Laura Greene

Abstract

Electronic, magnetic, and structural phase inhomogeneities are ubiquitous in strongly correlated quantum materials. The characteristic length scales of the phase inhomogeneities can range from atomic to mesoscopic, depending on their microscopic origins as well as various sample dependent factors. Therefore, progress with the understanding of correlated phenomena critically depends on the experimental techniques suitable to provide appropriate spatial resolution. This requirement is difficult to meet for some of the most informative methods in condensed matter physics, including infrared and optical spectroscopy. Yet, recent developments in near-field optics and imaging enabled a detailed characterization of the electromagnetic response with a spatial resolution down to 10 nm. Thus it is now feasible to exploit at the nanoscale well-established capabilities of optical methods for characterization of electronic processes and lattice dynamics in diverse classes of correlated quantum systems. This review offers a concise description of the state-of-the-art near-field techniques applied to prototypical correlated quantum materials. We also discuss complementary microscopic and spectroscopic methods which reveal important mesoscopic dynamics of quantum materials at different energy scales.

Keywords: strongly correlated electron materials, quantum materials, infrared spectroscopy, vanadium dioxide, near-field microscopy, mesoscopic physics, phase transitions, phase inhomogeneity

(Some figures may appear in colour only in the online journal)

Acronyms and abbreviations

AF	Antiferromagnetic	CO	Charge order
AFM	Atomic force microscopy	COO-I	Charge/orbital order insulating
ALS	Advanced light source	CMR	Colossal magnetoresistance
a-SNOM	Aperture based scanning near-field optical microscopy	DC	Direct current
CDW	Charge density wave	DDW	d-density wave
CL	Cathode luminescence	DFG	Difference frequency generation
CO-OO-AF	Charge and orbital ordered antiferromagnetic insulating state	DW	Domain walls
		FC	Field cooling
		HTSC	High temperature superconductors
		IR	Infrared
		KPFM	Kelvin probe force microscope

LPCMO	$\text{La}_{0.35}\text{Pr}_{0.275}\text{Ca}_{0.375}\text{MnO}_3$
MFM	Magnetic force microscopy
MIM	Microwave impedance microscopy
MR	Magnetoresistance
NMR	Nuclear magnetic resonance
NSMO	$\text{Nd}_{1/2}\text{Sr}_{1/2}\text{MnO}_3$
PCA	Photoconductive antenna
PDW	Pair density wave
PEEM	Photoemission electron microscopy
PSCMO	$\text{Pr}(\text{Sr}_{0.1}\text{Ca}_{0.9})_2\text{Mn}_2\text{O}_7$
QCLs	Quantum cascade lasers
SDW	Spin density wave
SINS	Synchrotron infrared nano-spectroscopy
S_n	Demodulated near-field signal at n th harmonic of the tip tapping frequency
SNOM	Scanning near-field optical microscopy
STM	Scanning tunneling microscope
s-SNOM	Scattering type scanning near-field optical microscopy
TEM	Transmission electron microscope
THz	Terahertz
V–O	Vanadium–oxygen
VO_2	Vanadium dioxide
V–V	Vanadium–vanadium
XRM	X-ray microscopy
YBCO	$\text{YBa}_2\text{Cu}_3\text{O}_{6+y}$
ZFC	Zero field cooling

1. Introduction: correlated quantum materials and their multi-scale complexities

Strongly correlated quantum materials encompass a wide class of systems in which interactions in the electronic system are essential for understating the exotic material properties that can't be described by the single electron band theory [1]. Charge, orbital, spin, and lattice degrees of freedom are entangled in these systems and compete at microscopic length scales, leading to complex emergent properties [2–5]. Examples of these properties include: numerous phase transitions and crossovers in correlated quantum matter, pseudogap state, non-Fermi liquid behavior, and quantum criticality phenomena [6–11]. The electronic system in many correlated systems is at the brink of the localization–delocalization transition, yielding rich and complicated phase diagrams. A common attribute of many classes of quantum materials is that these materials are susceptible to external perturbations such as temperature, strain, doping, electric- and magnetic-field. An incomplete list of correlated quantum materials includes unconventional superconductors, multiferroics, magnetoresistive manganites, organic and inorganic Mott insulators. Among these examples, transition metal compounds with partially filled d bands near the Fermi level are one of the most studied correlated systems. Conventional single-electron band theory usually predicts metallic behavior for such systems, while many of them are, as a matter of fact, Mott insulators at low temperatures [1, 12, 13]. Upon doping, Mott insulators reveal intriguing metal–insulator transitions and high T_c

superconductivity: the two phenomena at the focus of contemporary condensed matter physics.

A mounting body of evidence suggests that the complexities of correlated matter are often associated with the effects occurring at mesoscopic length scales. Minute modifications of the electronic and lattice structure in quantum materials can dramatically alter the ground state and result in the coexistence of multiple phases in the same crystals. In such cases, it is obvious that reductionism cannot be applied to infer fundamental physics [14] since the underlying complexities, especially those associated with intrinsic phase separation, are often irreducible and become important attributes of the system. Energy and/or momentum resolved spectroscopies can probe the electronic bands and elementary excitations with extreme sensitivity but are often incapable of revealing sufficient details of the phase complexities: area and time averaging obscures possible mesoscopic and metastable states. Therefore, scanning probe and imaging experiments carried out with proper spatial resolution are needed to advance the understanding of the underlying physics of correlated quantum matter.

Complementary to the spectroscopic and real-space signatures are insights from the time-domain. Characteristic time scales associated with the electron and lattice dynamics in correlated materials can span from femtoseconds to hours. Techniques with sufficient temporal resolution are able to selectively excite and probe particular electronic, magnetic, or lattice modes. Examples include time-resolved studies of quasiparticle dynamics in superconductors [11, 15–24], and heavy fermion compounds [25–29] as well as experiments on photo-induced superconductivity [30, 31], and insulator to metal phase transitions in vanadates [32–43], nickelates [44], manganites [45–51] and transition metal dichalcogenides [52]. We summarize some of the relevant effects in an energy-time-space diagram in figure 1. We point out that traditional time-domain measurements are carried out using diffraction limited methods and are subject to area-averaging. Inevitably, the important information regarding domain dynamics and microscopic metastable phase formation is smeared or lost. Therefore, a complete characterization of correlated quantum materials needs to be carried out with fine spatial, temporal, and spectral resolutions.

To meet the above-mentioned challenges, novel spatial and temporal probes are being developed to investigate different aspects of the electron and lattice behavior in correlated electron systems. Among them, modern infrared near-field imaging and spectroscopy techniques have combined the merits of traditional broadband IR spectroscopy and sub-diffraction optics. The low energy photons of THz and IR radiation (1 meV–100s meV) are inherently sensitive to the elementary excitations and collective modes of electrons and the lattice, enabling direct inquiry into the material properties such as the energy gap and superfluid density in high T_c superconductors, coherent quasiparticle peaks and anomalous spectral weight transfer in transition metal oxides. The fine spatial resolution down to ~ 10 nm permits the direct visualization of phase separation. The recent integration of ultrafast pump-probe with nano-scale spatial resolution is still in its infancy with the first encouraging results presented in [53–59].

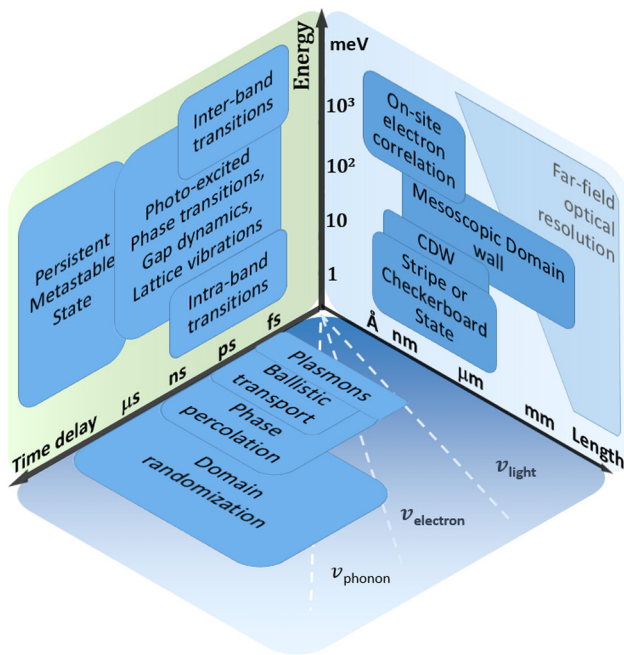


Figure 1. Space–time–energy schematic diagram: multiscale physics in strongly correlated quantum materials.

In this review we attempt to give a snapshot of mesoscopic physics in several classes of correlated quantum materials investigated via probing the electrodynamics of these systems with the nano-scale spatial resolution. The introductory section of this article is followed by a brief account of phase inhomogeneities in canonical correlated systems (section 2) and optical near-field infrared/optical techniques (section 3). Examples of near-field studies will be discussed along with the data obtained by complementary microscopy techniques (sections 4–6). Even though the roots of modern near-field nano-optics capabilities can be traced to the pioneering papers published in the 1980s and 1990s [60–67], only fairly recently have these methods emerged as a capable tool delivering new physical understanding of complex correlated electrons phenomena [68]. Recently developed new types of nano-optical characterization methods such as polariton interferometry [58, 69–80], thermal near-field spectroscopy [81, 82] and nano-photocurrent characterization [83], can all potentially be applied to enrich our present understanding of light–matter interaction in correlated quantum materials.

2. Hierarchy of length scales in inhomogeneous quantum matter

Phase separation and inhomogeneities are commonplace in strongly correlated electron materials. In one form or another, these effects have been observed in essentially every quantum material that has been studied with scanning probe methods offering atomic-, nano- and/or meso-scale spatial resolution. There are many different forms of inhomogeneities in correlated electron systems, especially in transition metal compounds with $3d$, $4d$ and f electrons. Figure 2 illustrates some of the relevant length scales and uncovers the propensity of correlated electron compounds towards the formation of

electronic and/or magnetic inhomogeneities. As one can see, the phase inhomogeneities and phase separation are spread over a wide range of length scales. In general, the formation and the length scales of the inhomogeneous states are governed by the interplay between the competing energy scales (e.g. Coulomb energy, kinetic energy, exchange energy, domain and surface energy) [3, 118], disorder [119–122] and frustration [123, 124]. We note that most of the references we list in the legend of figure 2 are directly related to microscopy techniques and are published in 2005–16.

A hierarchy of length scales associated with inhomogeneities is illustrated in figure 3. At the atomic level, one can identify *density inhomogeneities* associated with the variation of the electron or spin densities, or both. A variety of charge ordered (CO) [103, 109, 125–131], charge density wave (CDW) [18, 107, 112, 132–139], spin density wave (SDW) [7, 140–143], pair density wave (PDW) [144–148], and d-density wave (DDW) [149–157] ordered states as well as a plethora of charge and spin stripe states [4, 5, 158, 159] belong to this category. Scanning tunneling microscope (STM) and transmission electron microscope (TEM) have an outstanding track record of visualizing these inhomogeneities and unveiling their impact in the physical phenomena observed in correlated quantum materials.

The CDW-ordered or SDW-ordered states can extend over macroscopic dimensions, forming various types of domains or unidirectional stripes [4, 141]. When the rotational symmetry is broken, the stripes (or smectic phases) can segregate into nematic phases (figure 3(b)) [160]. This electronic nematic order is usually formed due to the density modulation along one unique direction and can be regarded as an electronic version of liquid crystals. However, unlike their molecular liquid crystals counterparts, the inherent instability of electronic nematic/smectic phases yields a high susceptibility to small perturbations such as crystal disorder. Typically, the domain sizes of nematic phases range from a few lattice spacings to tens of nanometers. The electronic nematicity has been reported for hole-doped cuprates [110, 161–171] and Fe-based high- T_c superconductors [109, 172–178]. Electronic nematicity is also believed to play an important role in the high T_c phenomenon. For example, the d-wave pairing and enhancement of superconductivity have been linked to nematic charge fluctuations near a quantum critical point [179, 180].

At even longer length scales, phase inhomogeneities are realized in the form of percolating domains (figure 3(c)). The mesoscopic pattern of the percolation and phase co-existence can be influenced by pressure (or other long range fields) and/or quenched disorder. Percolating domains are expected to occur in the vicinity of a sharp first order phase transition [3, 181–184]. Phase separation patterns in manganites, for example, can be strongly affected by the long-range strain field, where the local phases and length scales are believed to be determined by the energy of elastic strain mismatch and energies at domain boundaries [2, 3, 185–193]. Mesoscopic domains can extend to micrometer dimensions. The order parameters vary among domains (different conductivity, magnetization, lattice parameters, or band structures can co-exist at the same time but not necessarily have different charge

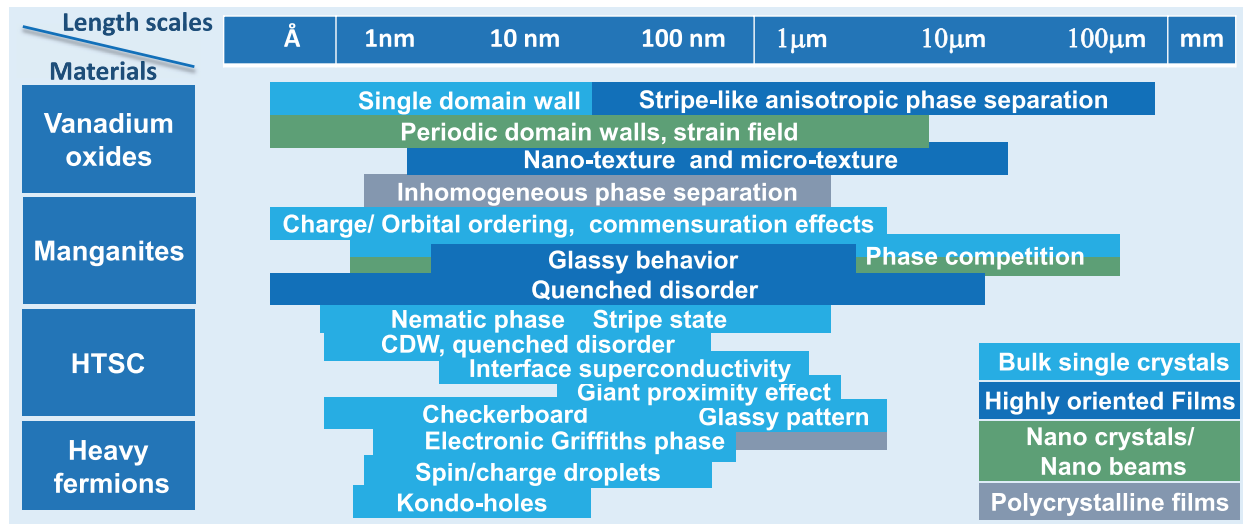


Figure 2. Representative correlated quantum materials along with the length scales of phase inhomogeneities and related mesoscopic phenomena. The color scheme represents different forms of the studied specimens: nanocrystals or nanobeams (green), highly oriented films (dark blue), bulk single crystals (sky blue) and polycrystalline films (grey). In vanadium oxides, phase separation between insulating and metallic domains has been visualized in single crystals [84–86], random phase percolation in high quality VO_2 and V_2O_3 films on sapphire substrates [68, 87] unidirectional stripe-like phase separation in highly oriented thin films [86, 88, 89] and periodic domain walls within VO_2 nanocrystals [90–92] or nanobeams [37, 93–102]. In manganites, charge/orbital ordering [103], quenched disorder [104], and glassy behavior [105, 106] have been observed. Mesoscopic phenomena in cuprates and Fe-based high temperature superconductors (HTSC) include charge density waves (CDW) [18, 107], stripe states [108], nematic phases [109], quenched disorder [110], checkerboards [111, 112], glassy states [113], interface superconductivity, and giant proximity effects [114]. In heavy fermion systems, experiments and theory revealed electronic Griffiths phases [9], spin/charge droplets [115] and Kondo holes [116, 117].

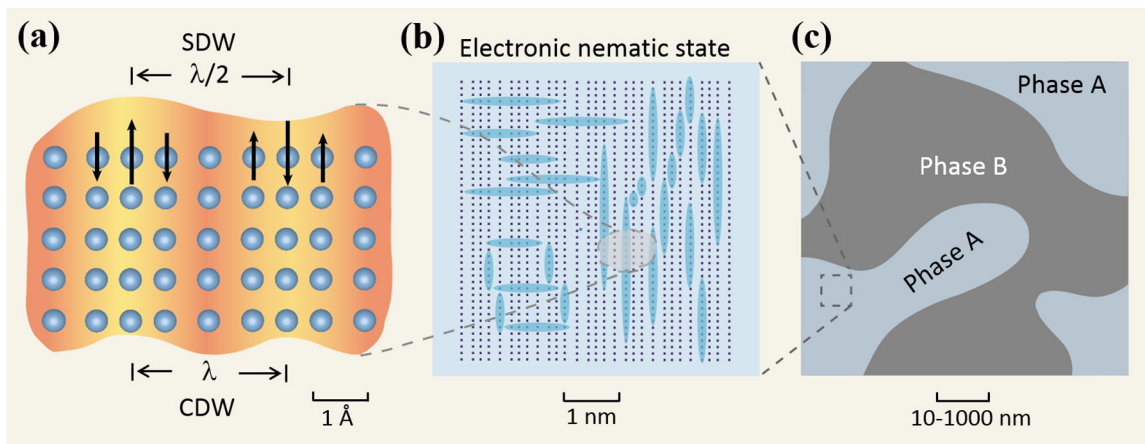


Figure 3. Schematic of multi-scale phase inhomogeneities [196–199] (a) spin density wave and CDW. Notice that the wavelength for SDW is double the wavelength for CDW. (b) Electronic nematic stripe state (c) mesoscopic scale phase percolation and phase inhomogeneities. Different phases with different electronic or lattice order can coexist in the nanometer to micrometer range.

density or electrochemical potentials), leading to a rich and variegated real space features in correlated materials [184].

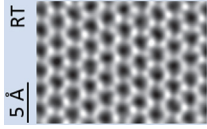
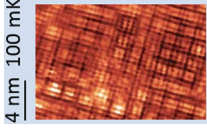
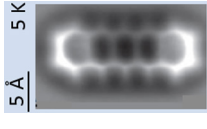
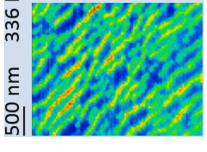
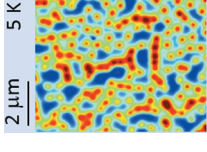
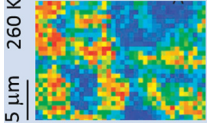
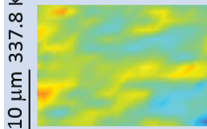
The origin of different types of phase inhomogeneities as well as the hierarchy of length scales in correlated quantum matter is a vibrant area of research. A prevailing opinion is that electron–electron and electron–lattice interactions play a major role [10], and the microscopic electronic phases are often related to the local variations of the crystal structure [190]. Multi-length scale physics is a common feature of correlated materials. Other well-known examples of large scale inhomogeneities in quantum materials include 2D electron systems of semiconductors at high magnetic fields in high mobility GaAs [194, 195].

3. Nano-scale near-field microscopy techniques

Numerous microscopy methods have been applied to visualize and characterize the hierarchy of phase inhomogeneities in quantum materials. Here we briefly summarize the contemporary microscopic techniques in table 1 [101, 200]. A thorough review of these techniques, their capabilities, and limitations is beyond the scope of this work.

The rise of near-field infrared/optical investigations of correlated quantum materials would not have been possible without recent advances in scanning probes and laser technologies. Important technical breakthroughs enabled ultra-stable and ultra-broadband light sources at IR frequency ranges, such as

Table 1. Contemporary imaging techniques with selected representative data.

Representative microscopy techniques	Transmission electron microscopy (TEM)	Scanning tunneling microscopy (STM)	Atomic force microscopy (AFM)	Scanning-type near-field optical microscopy (SNOM)	Magnetic force microscopy (MFM)	Photoemission electron microscopy (PEEM)	X-ray microscopy (XRM)
Lateral resolution	<0.1 nm	<0.1 nm	<1 nm	10 nm	10 nm	10 nm	30 nm
Dominant contrast	Electron density	Local density of states	Topography, atomic force	Drude response collective electronic excitations (plasmons, phonons)	Magnetic dipole-dipole interaction FM	Work function, absorption edge, FM, AF	Lattice structure, elemental composition
Representative image							

Note: (1) Transmission electron microscopy. Image shows aberration-corrected annular dark-field scanning transmission electron microscopy (ADF-STEM) of single layer graphene [201]. (2) Scanning tunneling microscopy (STM). Image shows conductance map of checkerboard patterns in a lightly hole-doped $\text{Ca}_{2-x}\text{Na}_x\text{CuO}_2\text{Cl}_2$ single crystal [202]. (3) Atomic force microscopy (AFM). Image shows the chemical structure of a pentacene molecule on $\text{Cu}(1\ 1\ 1)$ [203]. (4) Scanning near-field optical microscopy (SNOM). Image shows anisotropic stripe-like phase separation in a VO_2 film on TiO_2 substrate [88]. (5) Magnetic force microscopy (MFM). Image shows vortices in a single crystal $\text{Ba}(\text{Fe}_{0.95}\text{Co}_{0.05})_2\text{As}_2$ superconductor [204, 205]. FM: ferromagnetic. (6) Photoemission electron microscopy (PEEM). Image shows phase inhomogeneities in a $(\text{V}_{0.98}\text{Cr}_{0.01})_2\text{O}_3$ crystal [87]. AF: antiferromagnetic. (7) X-ray microscopy (XRM). Image shows intrinsic phase separation in a $\text{K}_{0.8}\text{Fe}_{1.6}\text{Se}_2$ single crystal [206]. See also a recent review on coherent x-ray imaging [207]. (1) Reproduced by permission from Macmillan Publishers Ltd: [201], copyright 2011. (2) Reproduced by permission from Macmillan Publishers Ltd: [202], copyright 2004. (3) From [203], reprinted with permission from AAAS. (5) Reproduced figure with permission from [204]. Copyright 2010 by the American Physical Society. (6) Reproduced by permission from Macmillan Publishers Ltd: [87], copyright 2010. (7) Reproduced figure with permission from [206]. Copyright 2011 by the American Physical Society.

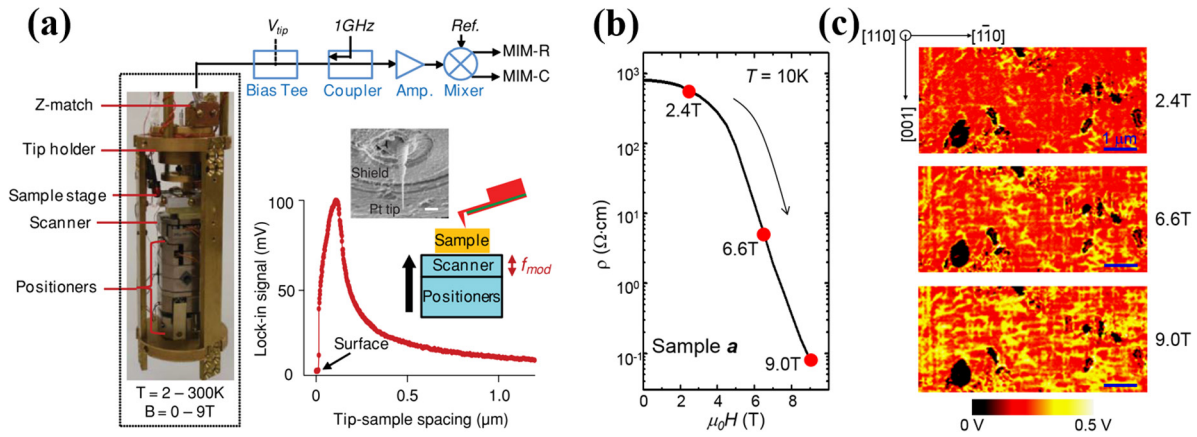


Figure 4. (a) Schematic of the low-temperature microwave impedance microscopy (MIM) setup [234]. Inset: A tip approach curve and a SEM picture of the shielded Pt tip. The scale bar is $2 \mu\text{m}$. (b) Magnetic field dependent resistivity of $\text{Nd}_{1/2}\text{Sr}_{1/2}\text{MnO}_3$ at 10 K [191]. (c) MIM images of $\text{Nd}_{1/2}\text{Sr}_{1/2}\text{MnO}_3$ at 2.4 T, 6.6 T, and 9.0 T (temperature at 10 K, scale bar = $1 \mu\text{m}$), corresponding to the dots in (b). Red: more insulating. Yellow: more conducting. (a) Reproduced with permission from [234], copyright 2011 AIP Publishing LLC. (b) From [191], reprinted with permission from AAAS.

quantum cascade lasers (QCLs) and high-repetition-rate ultrafast fiber lasers. These sources are capable of coupling sufficient infrared power to the tip-sample system such that the much smaller tip-scattered near-field signal is well above the noise floor of modern infrared detectors. Artifact-free imaging can be achieved with relatively easy optical setups and signal demodulation concepts (e.g. scattering type near-field setups and demodulation schemes, section 3.2). The development of novel detection schemes (e.g. pseudo-heterodyne detection) [208, 209] and quantitative analysis [210–214] also have helped to advance the technique. The commercialization of various types of near-field techniques fulfilling both academic and industrial needs has assisted the field as well. Synchrotron-based user facilities such as the synchrotron infrared nano-spectroscopy (SINS) implemented at advanced light source (ALS) in Lawrence Berkeley National Laboratory offer unique broadband nano-IR access to the international community [215]. Comprehensive reviews have been dedicated to the general topic of the optical near-field techniques [67, 101, 200]. In this section we only emphasize two different types of scanning near-field microscope techniques with different frequency ranges at ambient or low temperatures. We will discuss canonical examples of near-field and microscopic studies with high-quality samples of correlated quantum materials in sections 4 and 5.

Non-scattering near-field microscopy includes aperture-based optical near-field scanning microscopy (a-SNOM) [60, 216–225] and microwave impedance microscopy (MIM) [191, 226–235]. These methods require a waveguide-like structure to transmit the electromagnetic wave onto the AFM tip (section 3.1). Scattering type technique (s-SNOM), on the other hand, relies solely on free space propagation and on the demodulation of the scattered light from the AFM tip (section 3.2). Among the many advantages of s-SNOM we highlight the fact that the spatial resolution of this method is only limited by the curvature radius of the tip, which can be as small as 5–10 nm [236] or even 1–2 nm in the case tips terminated by carbon nanotubes. On the other hand, a-SNOM resolution is limited by the size of the tip aperture, which must be no

smaller than 50–100 nm to ensure adequate coupling of the near-field radiation. Both non-scattering type and scattering type near-field microscopy can operate over a broad range of frequencies from radio frequency, microwave, THz, Mid-IR to near-IR, and visible regions. Since aperture-based SNOMs are yet to find a broad utilization in correlated materials research, in this review we only discuss MIM and s-SNOM.

3.1. Microwave impedance microscopy (MIM)

MIM measures the effective tip-sample impedance [234] at microwave frequencies. It utilizes a sharp near-field probe, usually a specialized AFM tip, as an extension of transmission lines or waveguides that delivers propagating microwaves to the sample. The reflected microwave signal is sent back to microwave electronics through a $\lambda/4$ impedance matching scheme [234]. It yields two orthogonal output signals: real (MIM-Re) and imaginary (MIM-Im) parts of the impedance, corresponding to the loss and capacitive parts of the tip-sample impedance. The MIM technique requires special care since the tip has to be properly grounded and a reference phase has to be properly adjusted to read meaningful output signals. The wavelength is generally limited by the microwave electronics, which is typically in the 0.1 GHz (wavelength $\sim 3 \text{ m}$, energy $\sim 4 \times 10^{-7} \text{ eV}$) to 10 GHz ($\sim 3 \text{ cm}$, $\sim 4 \times 10^{-5} \text{ eV}$) frequency range. MIM can effectively probe the low energy material response, yielding the resistance and capacitance of a sample with a typical spatial resolution of 50–100 nm. The entire assembly can be integrated in an exchange gas or a flow cryostat, and can be placed in a superconducting magnet as shown in figure 4(a). This allows for temperature dependent (2–300 K) and magnetic field dependent (0–9 T) MIM imaging of correlated electron materials. Compared to conductive AFM, MIM provides a noninvasive approach at the low electromagnetic frequency range.

It is instructive to discuss the sensitivity of the microwave imaging. At the microwave frequency region, one can approximate the tip-sample system as an RC circuit (inductance L is omitted for open-circuit probes), empirically the optimal

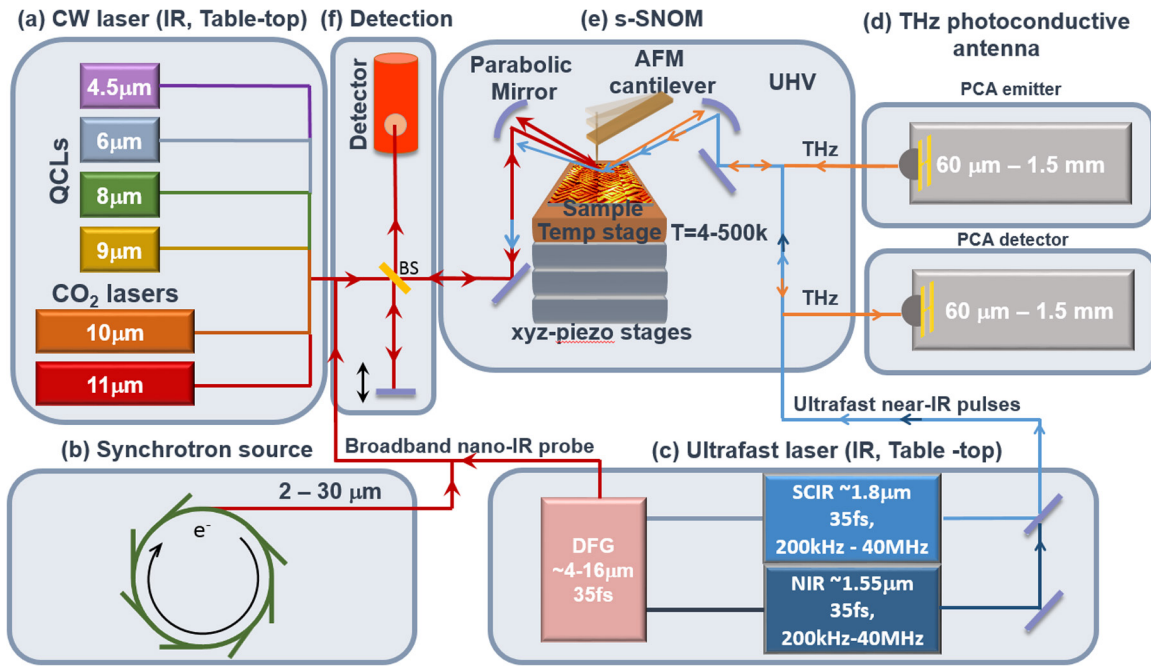


Figure 5. Schematics of scattering-type scanning near-field optical microscope (s-SNOM). (a) CW laser sources (b) ultra-broadband synchrotron light source (c) table top ultrafast broadband IR laser source (d) table top THz broadband sources utilizing photoconductive antennas (PCA) (e) AFM-based near-field platform with optics and sample stages. (f) Interferometric detection.

frequency for MIM with phase sensitivity is defined by the empirical formula $\omega RC \approx 1$, where ω is the microwave frequency, R and C are the effective tip-sample resistance and capacitance, respectively. From this relation one can find that for lower frequencies, microwave imaging is more sensitive to resistive samples with a higher resistivity. Therefore MIM operates over a range of about four decades centered around 1 S m^{-1} [234] (sheet conductivity around $1 \mu\text{S} \cdot \text{sq}$ for thin films [231, 237]), complementary to Mid-IR and far-IR near-field imaging techniques that are sensitive at higher conductivity ranges.

One of the first MIM applications in correlated materials research was a study of resistive networks in the manganite thin film $\text{Nd}_{1/2}\text{Sr}_{1/2}\text{MnO}_3$ (NSMO). A percolative phase transition from a charge/orbital order insulating (COO-I) state to a FM metallic state is observed at 10 K (figures 4(b) and (c)) [191]. The magnetic field dependent mesoscopic resistance network can be visualized by the MIM-Im signal, which has a monotonic dependence on the resistivity. COO-I domains are evident at low magnetic field while FM-metallic filaments percolate and continue to grow at higher magnetic fields. At 9 T the sample shows a large fraction of FM metallic state, which is aligned to specific crystalline orientations of the substrate. This liquid-crystal-like metallic network is confirmed to be electronic in origin as it is not apparent in the structural characterization. It is worth noting that the mesoscopic pattern can be tuned by field-cooling (FC) or zero field cooling (ZFC) processes (cooling the sample with and without applying a magnetic field, respectively). With the FC process one can observe larger conducting domains than those revealed in the ZFC scans, consistent with the hysteretic nature of the phase transition. The elastic strain plays a crucial role in the mesoscopically ordered network observed in NSMO, which

tends to expand along the strain-free axis, consistent with the in-plane anisotropy observed in the DC measurements. The percolative phase transition is believed to play a role in the observed phenomenon of colossal magnetoresistance (CMR) [118, 185, 187–189, 238], where the resistivity at a given temperature can change by several orders of magnitude with the application of a magnetic field [239]. The directionality of the domain growth has been observed in many correlated materials including vanadates, manganites, and superconductors as we will discuss below. More examples on MIM and manganites will be discussed in sections 5 and 6.

3.2. Scattering type SNOM (s-SNOM) and nano-IR spectroscopy

Scattering-type scanning near-field optical microscopy (s-SNOM) is an AFM based technique enabling sub-diffraction-limited studies of optical properties [66, 240]. It is a versatile method that allows nano-scale imaging and spectroscopy from terahertz frequencies to visible wavelengths and at variable temperatures [101, 200, 240, 241]. Naturally, s-SNOM inherits all the features of AFM including various modalities of topographic imaging. Additional modes including MFM, Kelvin probe, and conducting AFM can be implemented in an s-SNOM setup. Figure 5 shows a schematic for a state-of-the-art s-SNOM adapted for broadband spectroscopy and ultrafast pump probe capabilities.

The sources of radiation in modern s-SNOM are CW or ultrafast lasers. The detection of the scattered signal requires high NA focusing optics (lens or parabolic mirror, figure 5(e)), a reference arm (an asymmetric interferometer) and a relatively fast ($>2 \text{ MHz}$) detector. The reference arm is used to multiplicatively enhance and phase-reference the

detected near-field signal with homodyne or *pseudo-heterodyne* detection (figure 5(f)), yielding the amplitude and phase of the near-field signal. In a typical setup, a CW or broadband laser beam can be focused onto a metalized (metal coated or semiconducting) AFM tip and the back-scattered signal (S_n) is demodulated at higher harmonics of the tip's tapping frequency ($n = 2, 3, 4, \dots$). These higher harmonic signals (S_2 – S_4) contain information about the local dielectric function with suppressed topography-induced artifacts [211, 242–245]. In a typical table top experiment, QCL or gas lasers are employed as monochromatic IR light sources (with moderate frequency tuning, figure 5(a)). IR and THz pulses generated from ultrafast lasers can be used as coherent broadband probes [246] (figures 5(c) and (d)). The center frequency range of IR pulses produced via difference frequency generation (DFG) method in a nonlinear crystal (e.g. GaSe) is tunable from $\sim 700\text{ cm}^{-1}$ to $\sim 2200\text{ cm}^{-1}$ with a typical bandwidth of $\sim 250\text{ cm}^{-1}$ (full bandwidth ~ 4 – $16\ \mu\text{m}$). THz pulses generated from photoconductive antennas can cover a 0.2 THz–5 THz frequency ranges ($\sim 60\ \mu\text{m}$ – 1.5 mm , figure 5(d)). Synchrotron-based national facilities (figure 5(b)) such as the SINS at ALS Berkeley yield ultra-broadband nano-IR capabilities with a typical bandwidth from 350 – 4500 cm^{-1} (~ 2 – $30\ \mu\text{m}$) [215]. Spectra of the amplitude and phase of tip-scattered fields in aforementioned broadband sources can be obtained via asymmetric Michelson interferometric detection, analogous to conventional Fourier transform spectroscopy [211, 215, 242]. In addition, with coherent light pulses, amplitude and phase information can also be obtained simultaneously from time domain measurements via e.g. electro-optical sampling, which was recently demonstrated in reference [55]. The flexible geometry and the novel way of demodulating scattering signals ensure that s-SNOM provides exquisite optical imaging and broadband spectroscopy capabilities with a spatial resolution limited only by the apex radius of the AFM tip [247].

Near-field optical techniques can be extended to the time-domain by utilizing the ultrafast pulses as light sources. A near-field pump-probe experiment is suitable for real-time nanoscale characterization down to $\sim 20\text{ nm}$ combining with $\sim 20\text{ fs}$ temporal resolution [53–59]. The combined ultrafast and near-field optics platform offers an opportunity to harness photoexcited dynamics in the search for hidden phases in quantum materials where local inhomogeneities are omnipresent [37, 68, 76, 86, 88, 89, 100, 191, 244, 248, 249]. This line of inquiry critically depends on yet another experimental capability: cryogenic operation. Cryogenic infrared (IR) near-field imaging is challenging: in order to prevent surface contamination (e.g. water layer adhesion) at low temperature, an ultra-high vacuum environment is mandatory. Current state-of-the-art cryogenic s-SNOM has been demonstrated to operate in a $\sim 20\text{ K}$ – 500 K temperature range [250] in a $\sim 10^{-9}$ mbar UHV environment. Although not the main topic of this review, we wish to emphasize that near-field techniques also allow access to finite momenta: a natural consequence of light scattering off the AFM tips [249]. Finite momentum coupling is indispensable for studying plasmonic and polaritonic effects in quantum matter. So far these polaritonic effects have been investigated in graphene and other 2D materials [69–78, 251]

but are yet to be experimentally explored in systems with correlated electrons [252].

4. Near-field imaging and spectroscopy of phase separation in vanadium oxides

VO_2 is a strongly correlated phase change material with an insulator to metal phase transition (IMT) temperature at $T_{\text{IMT}} \sim 340\text{ K}$ [253]. The phase transition leads to a ~ 4 – 5 orders of magnitude change in conductivity. Accompanying the IMT, there is a structural phase transition (SPT) in which the crystal symmetry changes from a monoclinic state to a rutile state with V–V dimerization [254, 255]. Vanadium dioxide (VO_2) was the first and most extensively studied correlated system with nano-optical methods [68]. Numerous publications dedicated to VO_2 attest to the rich physics associated with the IMT and phase separations that can be uncovered with nano-IR experiments [37, 68, 86, 88–93, 95–98, 256–263]. The origin of the IMT in VO_2 has been debated for decades. While it is certain that both Mott and Pierels physics play a role in IMT, it was only recently that evidence suggested the separation of the electronic and lattice phase transitions at the nano-scale [88, 257, 260]. Femtosecond time-resolved spectroscopy also reveals that VO_2 band gap collapses with photo-excitation in the absence of a structural bottleneck [34, 264], supporting electronically driven IMT [265]. New evidence from nanoscale probes indicates that many of the discrepancies found by comparing different measurements might originate from mesoscopic inhomogeneity in samples under investigation. Here we discuss a few recent reports on phase separation in VO_2 studied via near-field imaging.

4.1. Electronic phase separation in VO_2

Figure 6 shows near-field imaging of phase inhomogeneity patterns observed in different forms of VO_2 including films (figures 6(a), (d) and (e)) [68, 88, 89], microcrystals (figure 6(b)) [37] and nanoplatelets (figure 6(c)) [91]. It is evident that near-field microscopy is a versatile technique capable of studying all of the above sample forms. Nano-IR methods can even access the cross sections of thin film samples (figure 6(e)) [89]. These measurements are acquired at IR and microwave frequency ranges which effectively probe the Drude conductivity tail associated with correlated electrons [68]. We note the brighter color (such as white, red or golden) represents a more metallic response by convention while the darker color (such as black and dark blue) represents a more insulating response.

Figure 6(a) shows the first IR near-field study of a correlated electron system. This plot evidently demonstrates the nucleation and growth of metallic regions during a thermally induced phase transition in a VO_2 film on sapphire substrate [68]. This work has generated substantial interest and evoked a wave of enthusiasm to search for phase inhomogeneities and related memory effects in VO_2 and other related materials by means of nano-IR methods.

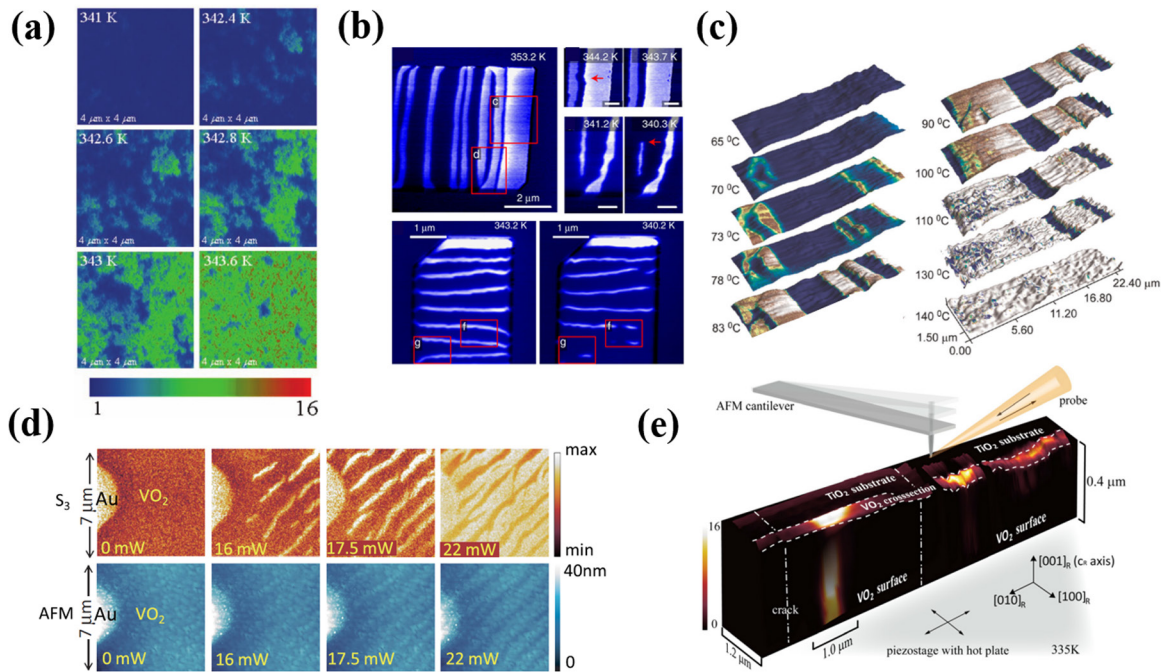


Figure 6. (a) Temperature dependent IR near-field images of VO₂ film on a sapphire substrate (341–343.6 K) [68]. Image size: 4 × 4 μm. Infrared frequency $\omega = 930\text{ cm}^{-1}$. Red: metallic phase. Blue: insulating phase. (b) Temperature dependent IR near-field images of VO₂ microcrystals [37]. Alternating metallic (white) and insulating (blue) domains form perpendicular to the c_R axis of the microcrystals. Domains can be irregular and shrink to small metallic puddles close to the phase transition temperature. The IMT is probed by a 10.8 μm CO₂ laser. (c) Temperature dependent MIM images of VO₂ nanoplatelets [91] (65–140 °C). White regions signify high conducting metallic state and blue is insulating. (d) Unidirectional phase separation in a VO₂ film on a [1 1 0]_R TiO₂ substrate, measured by IR near-field imaging [88]. The samples are thermally heated by a near-IR pump laser (at ~1.5 μm). Top row: IR scattering amplitude S_3 recorded at distinct power levels of the pump laser. Bottom row: sample topography (AFM) for the images displayed in the top row. The center frequency of the probe beam is ~1100 cm⁻¹. (e) IR Near-field image of the VO₂/[1 0 0]_R TiO₂ cross-section at 335 K [89]. The VO₂ film thickness is ~250 nm. (a) From [68], reprinted with permission from AAAS. (b) Reproduced by permission from Macmillan Publishers Ltd: [37], copyright 2015. (c) Reproduced with permission from [91], copyright 2010 American Chemical Society.

Figure 6(b) displays IR near-field imaging of the thermally induced IMT in VO₂ microcrystals with thicknesses of 25–200 nm. The metallic domains are formed perpendicular to the rutile c axis (c_R axis) to minimize the free energy associated with the substrate-induced strain. The highly inhomogeneous IMT behavior in a seemingly homogeneous single crystal reveals the fact that defects, intra-crystal inhomogeneity and spontaneous strain formation is crucial in determining the microscopic domain pattern and it is a highly dynamic process when the temperature is close to T_{IMT} [37]. Figure 6(c) reports the formation of domains in nanoplatelets of VO₂ measured by MIM working in the contact-AFM mode (the microwave frequency was tuned to 1.78 GHz). It is found that upon heating, existing metallic regions can reenter the insulating (semiconducting) phase, indicating important long-range elastic interactions with domain boundary movement (for example, at 130 °C in figure 6(c)). This study reveals the importance ferroelastic behavior where the Ginzburg–Landau approach can be used to consider the general rules of phase transitions in nanomaterials with epitaxial strain.

Figure 6(d) displays an IR near-field study of a VO₂ thin film on a [1 1 0]_R TiO₂ substrate. In order to perform experiments at elevated temperatures, an optical pump beam centered at the near infrared wavelength of 1.5 μm was used to thermally excite the sample. To properly reference the near-field signal, lithographically patterned gold pads were deposited on the sample to enable *in situ* sample-reference scans within the same

scan window (to the left of each image in figure 6(d)). It was found that with the optical pump, one can generate local heating with a similar effect as increasing the temperature while providing more stable AFM and s-SNOM performance. As shown clearly in the first row in figure 6(d), a highly stripe-ordered pattern with unidirectional domains running along [1 $\bar{1}$ 0]_R was observed. The density and width of these stripes increased with increasing pump intensity. The key finding was that the macroscopic anisotropy of the film is intimately related to the phase separation at microscopic scales. Electronic anisotropy as measured by DC, far field IR or THz measurements with a large detection area yield a highly anisotropic conductivity (up to $\sigma_b/\sigma_c = 50$) due to the averaging effect over the observed unidirectional in-plane phase separation. The phase separation is also found in cross sections of the samples where the strain field varies across the depth of the sample (figure 6(e)).

Near-field results provide a unique real space perspective for the tunable macroscopic dynamics in VO₂ films. It is useful to summarize the emerging trends of the mesoscopic patterns in VO₂ samples, especially for those in bulk crystal and thin film forms since they are widely accessible. Figure 7 illustrates differences between bulk VO₂ crystals and highly oriented VO₂ film behavior, investigated by nano-IR imaging at ~1000 cm⁻¹. The left panel presents actual data (top view) and the right panel provides simplified schematic drawings (side view). It is evident that bulk crystals, VO₂/sapphire films

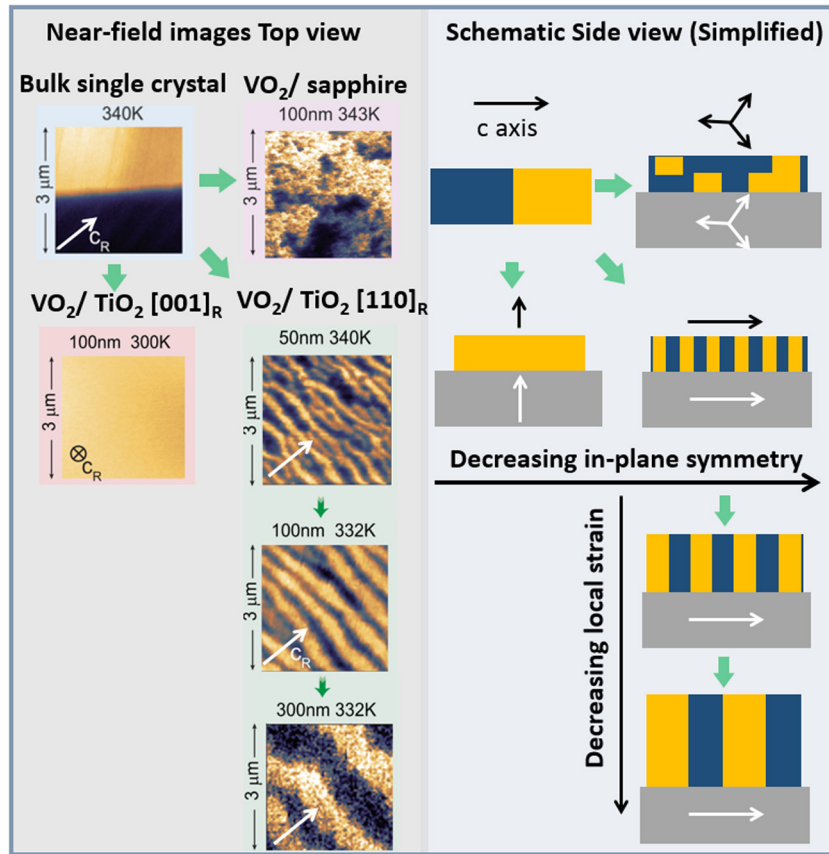


Figure 7. VO₂ phase separation diagram [86, 88, 89]. Left: near-field images (top view) on VO₂ bulk single crystal, VO₂ on sapphire and [110]_R and [001]_R TiO₂ substrates. Golden (blue) color represents the metallic (insulating) state. The probe wavelength is centered at $\sim 10 \mu\text{m}$. Images are all $3 \mu\text{m} \times 3 \mu\text{m}$. Film thicknesses and temperatures are indicated on the top of each image. Right: schematic side view of the crystal/substrate symmetry and strain (in this case film thickness) dependent phase separation in VO₂, with each position corresponding to the images in the left panel.

and VO₂/TiO₂ films show distinct mesoscopic patterns in the vicinity of IMT. For VO₂ bulk crystals, a sharp insulator–metal phase boundary is observed between the monoclinic and rutile phases. For high-quality VO₂ films on sapphire substrates, complex phase percolation can be observed and depicted by the random field model [68, 266]. For highly oriented VO₂ films on [110]_R TiO₂ with in-plane c_R -axis, self-organized patterns are evident. In VO₂/TiO₂ [110]_R films, alternating compressive and tensile strain yields interesting stripe-like patterns due to the epitaxial strain mismatch and VO₂ symmetry breaking [35, 50]. For highly oriented VO₂/TiO₂ [001]_R films with an out-of-plane c_R -axis, a uniform and gradual phase transition pattern is observed. This dramatic change in near-field patterns observed among different VO₂ samples signifies a process of phase separation mediated by local strain and crystal symmetry [86]. This systematic observation can serve as a starting point for understanding correlated quantum materials under epitaxial strain via near-field methods. To further elucidate details of the lattice and electronic states that occur with phase inhomogeneities, one needs to obtain spectroscopic data augmenting the near-field images collected at the selected frequencies. Broadband nano-IR spectroscopy is therefore well poised to reveal spectroscopic signatures that are representative of the structural

and electronic properties with the same spatial resolution as the near-field images.

4.2. Near-field infrared spectroscopy of structural and electronic phase transitions in VO₂

The ability to obtain local optical spectra with 20nm resolution is invaluable to material research. As previously introduced in section 3, infrared nano-spectroscopy can be performed with state-of-the-art table-top and synchrotron facilities, providing direct access to electronic and vibrational features. Initial efforts have been conducted with both sources to study the phase transitions in VO₂ thin films. These experiments were motivated by the challenge to investigate the interplay between the electronic and structural phase transitions.

The initial efforts of nano-IR studies of VO₂, although limited by the available IR bandwidth, are stimulating and suggestive. In films with an in-plane c_R axis where individual metallic islands can be spotted, a separation of lattice dynamics and electronic behavior at $\sim 100\text{nm}$ length scales can be identified (figure 8(a)) [88]. However, in thin films with an out-of-plane c_R axis where no obvious domain boundaries are observed, the film is mostly clamped by the epitaxial strain and the electronic structure and lattice structure show

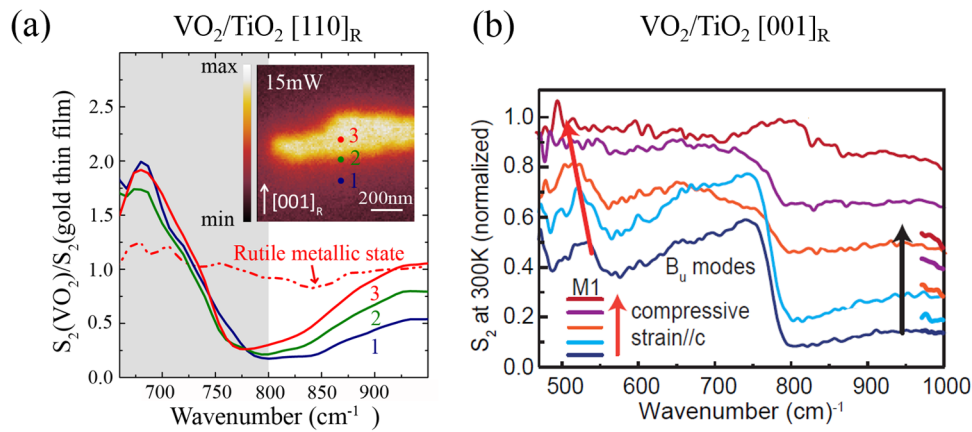


Figure 8. (a) Near-field spectra from three selected locations around a metallic island in the inset image of near-field amplitude. Reproduced with permission from [88]. Copyright 2015 by the American Physical Society. The sample is a 300 nm VO_2/TiO_2 [110]_R film. (b) Normalized nano-IR spectra S_2 taken at five representative locations on a 30 nm VO_2/TiO_2 [001]_R film [86]. The five locations are chosen to be with increasing local compressive strain along c_R axis (increasing strain from bottom to top, indicated by the arrows. For clarity, the curves in (d) are shifted vertically. The high-frequency end of the un-shifted data is also plotted at $\sim 950\text{--}1000\text{ cm}^{-1}$.

synchronized shifts (figure 8(b)) [86]. These results are achieved by simultaneously monitoring the local metallicity at $\sim 1000\text{ cm}^{-1}$ and local IR active phonon modes at below $\sim 700\text{ cm}^{-1}$ in a $\sim 20 \times 20\text{ nm}^2$ area. The experimental results suggest that the intermediate metallic states likely exist at the early stages of the phase transition due to epitaxial strain or defects. In this peculiar intermediate state electronic IMT is shown to precede the structural phase transition, as shown in figure 8(a) (also see reference [248, 257, 265]).

To further scrutinize the role of V–V and V–O bonds in VO_2 and draw a conclusive picture of the electron-lattice correlation, a broader IR bandwidth is required to access the entire set of the IR active modes. Nano-IR spectroscopy and nano-imaging at a wide spectral range (e.g. $100\text{ cm}^{-1}\text{--}5000\text{ cm}^{-1}$) is a technique of choice for this line of inquiry. Other collective electronic modes such as polaronic and excitonic responses can also be extensively investigated in correlated quantum materials in well-defined strain or geometrically confined environments.

5. Phase separation and nano-imaging in manganites

Manganese oxides, or manganites, have been a field of intense study for decades due to their extraordinary electronic and magnetic properties. The study of manganites has brought forward important concepts in modern condensed matter physics such as Jahn–Teller distortion [267–273] and double exchange interaction [274–278]. These extraordinary properties often originate from the interplay between the strong correlation of the $3d$ -electrons and the itinerant properties of doped holes. Manganites received renewed interest in 1990s following several milestone discoveries: for example the large magnetoresistance (MR) effects in $\text{Nd}_{0.5}\text{Pb}_{0.5}\text{MnO}_3$ [279] and $\text{La}_{2/3}\text{Ba}_{1/3}\text{MnO}_x$ [280] and CMR effect in 1994 [239].

The perovskite lattice structure of manganites is referred to as having a crystal structure related to the mineral perovskite CaTiO_3 (an ABO_3 structure with manganese atom surrounded

by six oxygen atoms to form a MnO_6 octahedron). The trivalent rare earth and/or divalent alkaline earth cations serve as electron or hole reservoirs for the Mn–O bonds. When doped, the double exchange interaction and electron lattice interaction (Jahn–Teller) compete to set the $3d$ electrons at the brink of the localization and delocalization. For example, the CMR manganite compound LaMnO_3 ($\text{Mn}^{3+} + (t_{2g}^3 e_g^1)$) has an anti-ferromagnetic insulating ground state. With appropriate doping such as Ca^{2+} or Sr^{2+} , it establishes a mixed valence state ($\text{Mn}^{3+}/\text{Mn}^{4+}$) with many different types of phase transitions occurring over a wide temperature range, such as in the case of $\text{La}_{1-x}\text{Ca}_x\text{MnO}_3$.

The first piece of evidence of phase coexistence in manganites ($\text{La}_{1-x}\text{Ca}_x\text{MnO}_3$) came from neutron scattering studies in 1955 [281], only 5 years after the first discovery of the novel DC and magnetic behavior of the materials [282, 283]. Phase coexistence was later confirmed with numerous techniques such as noise measurements [284] micro x-ray diffraction [285, 286], nuclear magnetic resonance (NMR) [287], and Mossbauer spectroscopies [288]. The first experimental work to show a direct visual of the electronic inhomogeneities was a TEM study of charged stripes in $\text{La}_{1-x}\text{Ca}_x\text{MnO}_3$ thin films [126], followed by works with other types of high resolution imaging techniques, such as dark field images [185], STM [289–291], MFM [105], and PEEM [106]. Numerous theoretical efforts as well as several reviews on the subject of phase coexistence have been published [2, 3, 189, 190, 196, 292, 293]. To date, the phase coexistence and inhomogeneities in manganites have been firmly established and are believed to be due to the similarity of the free energy scales of different phases. However, on account of defects or strain, the phase separation cannot be simply explained by local and global energy minima as addressed in numerical simulations [190, 292]. The effects of short- and long- range lattice distortion must be considered as well.

One example of a near-field study of doped manganites is given in figure 9, where MIM is performed at above room temperature to identify the domain walls (DW) in

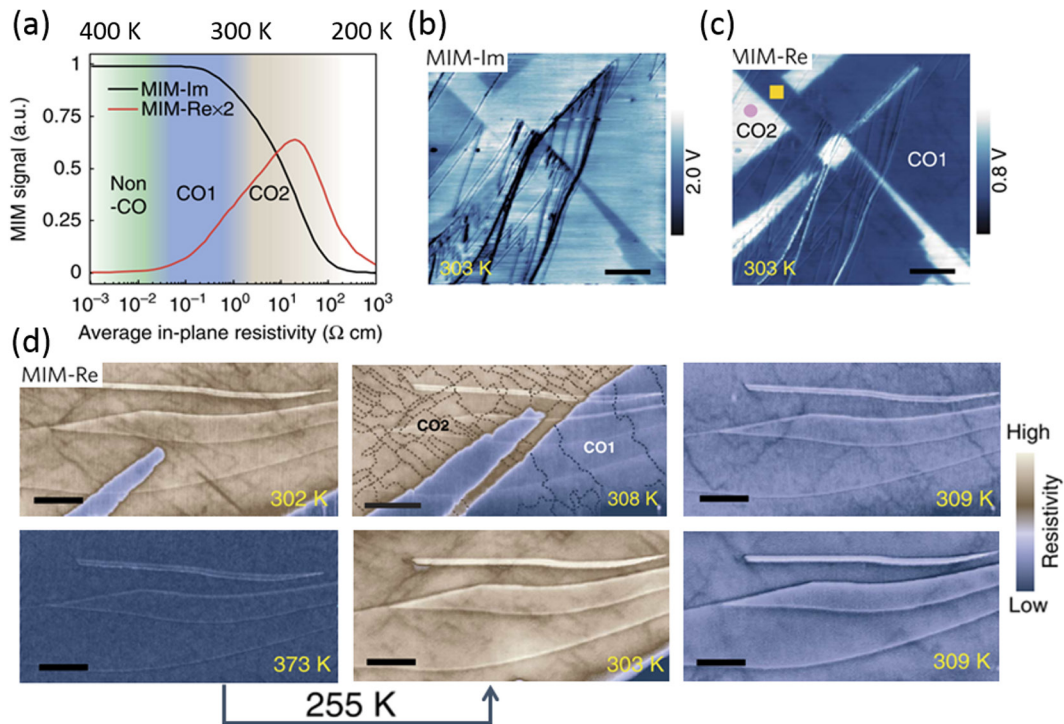


Figure 9. MIM study of layered manganite $\text{Pr}(\text{Sr}_{0.1}\text{Ca}_{0.9})_2\text{Mn}_2\text{O}_7$. Reproduced by permission from Macmillan Publishers Ltd: [103]. Copyright 2015, CC BY 4.0 (a) The temperature and resistivity dependence of MIM-Im and MIM-Re signals. (b) MIM-Im (c) and MIM-Re images of CO1 and CO2 phase coexistence, respectively. Scale bars in (b) and (c) are $5 \mu\text{m}$. (d) Temperature dependence of charge-order domain walls and domain boundaries with enhanced conductivity observed by high-contrast MIM-Re imaging. Scale bars in (d) are $3 \mu\text{m}$.

$\text{Pr}(\text{Sr}_{0.1}\text{Ca}_{0.9})_2\text{Mn}_2\text{O}_7$ (PSCMO). The layered manganite PSCMO reveals a non-charge-ordered phase at high temperature ($>370\text{K}$) and two charge-ordered states at relatively at lower temperature: CO1 below $\sim 370\text{K}$ and CO2 state below $\sim 303\text{K}$ [103]. As shown in figure 9(a), when the temperature decreases (top horizontal axis), the average in-plane resistivity increases with the emergence of CO1 and CO2 phases. Since the real and imaginary part of the MIM pick up the resistive and capacitive responses of the tip-sample interaction, respectively, they have different responses to the average in-plane resistivity. Since CO1 phase has a lower resistivity, the MIM-Im signal is higher in the CO1 phase, as shown in figures 9(a) and (b). It is worth emphasizing that unlike IR near-field imaging, the MIM-Re signal is non-monotonic with the resistivity and while the MIM-Im response is monotonic. Therefore, in order to map the charge ordered phases and the domain walls with reliable contrast MIM-Re signal is chosen only at monotonic regions above 300 K (figures 9(a), (c) and (d)). Even though the DW can be as narrow as several nm as predicted by finite element analysis, they can nevertheless be picked up by the MIM signal with $\sim 100\text{nm}$ resolution (figure 9(d)). The DW also show preferential orientation along certain axis ($a \pm b$) where the conductivity is enhanced compared to the adjacent domains due to the local lifting of the CO phases. The density of the DW also differs in different CO phases: in the CO2 phase is denser, as shown in figure 9(d).

Figure 10 shows a PEEM study of $\text{La}_{0.35}\text{Pr}_{0.275}\text{Ca}_{0.375}\text{MnO}_3$ between 48 K and 138 K with x-ray magnetic circular dichroism (XMCD) [106]. The charge- and orbital-ordered antiferromagnetic insulating state (CO-OO-AF) coexists with

the ferromagnetic metallic (FM) domains. As the temperature decreases, FM domains arise out of the CO-OO-AF background together with a clear thermal hysteresis. This phase coexistence is considered to be a direct result of the glassy nature of the charge and orbital order in the CO-OO-AF phase, as confirmed by PEEM and resonant elastic soft x-ray scattering (RSXS). This mesoscopic phase texture in $\text{La}_{0.35}\text{Pr}_{0.275}\text{Ca}_{0.375}\text{MnO}_3$ is in stark contrast to the previously discussed results in PSCMO, which has no FM order [294].

Besides thin films and bulk crystals, recent experiments in LPCMO microbeams/microcrystals have demonstrated phase separation domains and edge states ranging between tens to hundreds of nanometers. The formation of nanometer size domains can be clearly detected by the abrupt resistance change upon increasing temperature (figure 11(a)) in DC measurements. This type of domain separation has been visualized with cathode luminescence (CL) imaging using scanning electron microscopy [296]. As shown in the figure 11(b), the integrated sum of CL intensities unambiguously demonstrated that the nanoelectric domains with single domain sizes in LPCMO are 70–200 nm. Notice that with different CL intensity integration ranges (450 nm–520 nm and 680 nm–750 nm), the contrast of the image is opposite in LPCMO (middle and bottom image in figure 11(b)). Edge states have also been identified in LPCMO under high magnetic field [297]. Figure 11(c) demonstrates distinct appearance of the ferromagnetic (FM) metallic state along the edge of the LPCMO stripes under 9 T using magnetic force microscopy (bright contrast at 10 K in figure 11(c)). This pronounced mesoscopic ferromagnetic edge phase displays a ferromagnetic

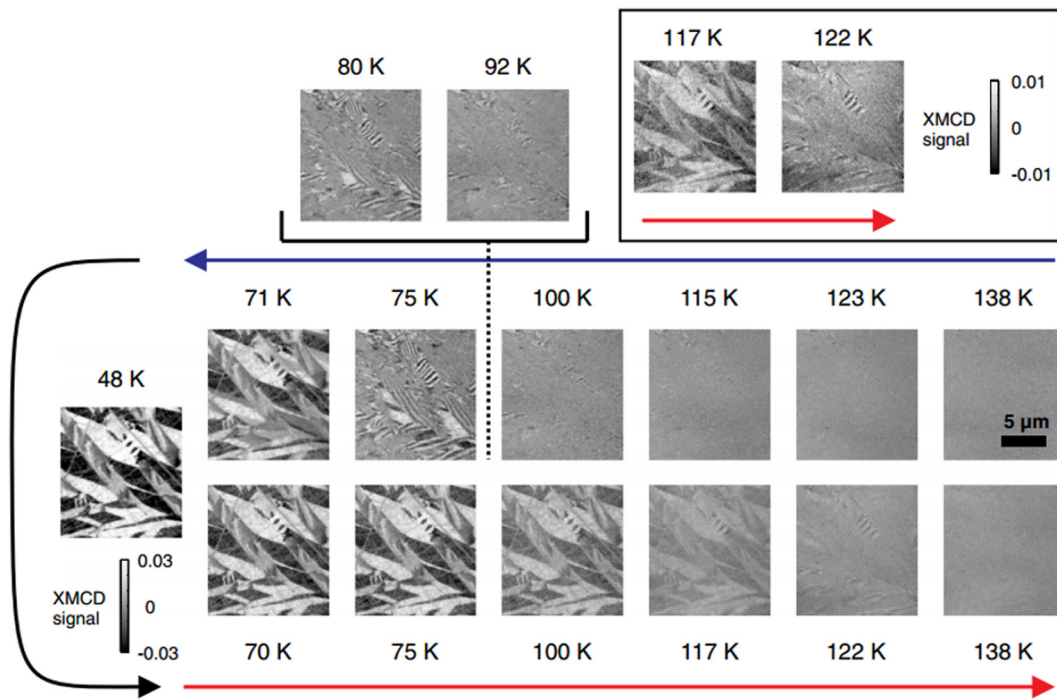


Figure 10. PEEM XMCD images of $\text{La}_{0.35}\text{Pr}_{0.275}\text{Ca}_{0.375}\text{MnO}_3$ taken from 138 K to 48 K showing hysteresis. Between 75 K and 100 K, alternating FM stripes dominate the micro texture. Reproduced figure with permission from [106]. Copyright 2012 by the American Physical Society.

signal 10 times larger than that of the electronic phases inside the strip and is expected to be seeded at the nanometer scale.

Despite the well-documented studies of mesoscopic physics in manganites, methods capable of simultaneously monitoring the electronic, magnetic, and lattice structure are still lacking at this stage. A broadband nano-IR setup with a magnetized tip can realize AFM, MFM, and near-field IR imaging & spectroscopy within a single measurement. Therefore, combined with the low temperature capabilities, the IR s-SNOM technique is potentially well suited for affirming the relation between the magnetic (especially ferromagnetic) or electronic phase transitions and their correlation with the structural changes. Cryogenic near-field IR measurements are needed for nano-characterization of various types of low temperature phases in manganites, together with other novel transition metal compounds such as high T_c superconductors, iridates, and osmates.

6. Domain formation and domain boundaries in iridates and osmates

Although relatively unexplored, iridates, either in the form of the Ruddlesden–Popper series ($\text{Sr}_{n+1}\text{Ir}_n\text{O}_{3n+1}$) or in the pyrochlore form ($\text{A}_2\text{Ir}_2\text{O}_7$, where A = yttrium or a lanthanide element), have drawn much attention recently due to the abnormal properties arising from strong spin–orbital coupling and e–e correlation. In the case of the Ruddlesden–Popper series, IR spectroscopy reveals that the Mott–Hubbard bandwidth W increases as n increases from 2 to ∞ , leading to an insulator to metal transition [299]. In the case of pyrochlore iridates, for example $\text{Nd}_2\text{Ir}_2\text{O}_7$, an IMT at the Neel temperature $T_N \sim 32$ K can occur with an unusual Ir magnetic moment arrangement.

The Ir moments either points to or points away from the centers of corner-sharing tetrahedron, forming an ‘all-in–all-out’ (or all-out–all-in) magnetic order at low temperature insulating phase [298, 300–304] (figure 12(a)).

The all-in–all-out (AIAO) and all-out–all-in (AOAI) domains in $\text{Nd}_2\text{Ir}_2\text{O}_7$ are found to be extended to micrometer sizes with highly conductivity domain walls, as being confirmed with MIM-Im imaging (figures 12(c) and (d)). The formation of these conductive domain walls can be regarded as the origin of the conductive features of the untrained samples at low temperatures and the step like conductance change under the high magnetic field up to 9 T (figure 12(b)).

The IMT and AIAO/AOAI magnetic order have been demonstrated in other types of pyrochlore oxide compounds as well. For example, osmium pyrochlore oxide $\text{Cd}_2\text{Os}_2\text{O}_7$ is well known for its abrupt IMT at ~ 227 K [305]. This second order IMT accompanied by a concurrent phase transition in magnetic order [306] has been previously studied by optical spectroscopy [307, 308] and only recently has been interpreted as a Lifshitz-type transition [308, 309]. It is plausible that the IMT is induced by AIAO ordering [310–312], where no doubling of a magnetic unit cell is needed. The AIAO magnetic domain structure is directly observed in real space with high resolution x-ray micro-diffraction performed at the Os L_3 absorption edges (10.871 keV) [313]. Interestingly, the magnetic domain distribution can be controlled by the orientation of the applied magnetic field, despite that fact that the magnetic domains are antiferromagnetic [313].

The similarities in the iridates and osmium compounds seems to suggest a rather universal magnetic domain behavior in $5d$ pyrochlore oxides [303, 309]. In future studies broadband IR near-field investigations can be unutilized to determine the evolution of the band shifts within single magnetic

domains. It can be worthwhile to investigate dynamics of highly conductive and mobile domain walls by means of near-field optical pump probe experiments.

7. Looking into the future

Examples of static nano-scale imaging of vanadates, manganites and iridates with infrared nanoscopy and other complementary nano-scale techniques attest to the high potential of these methods for studies of correlated quantum matter. Similar detailed studies of the nano-scale phenomena are yet to be achieved in other types of correlated systems. Numerous other systems including cuprate and ion-based high- T_c superconductors still await examination at nano- to meso-oscopic length scales. In this section we highlight several possible directions for where static IR near-field imaging techniques are likely to produce a major impact.

Apart from the static measurements, ultrafast nano-imaging and nano-spectroscopy will allow one to examine the photo-induced phase dynamics with subdiffractional spatial resolution. Initial ultrafast near-field experiments have been recently reported for graphene [53, 58], III–V semiconductors [54, 55] and VO_2 [56, 57]. In section 7.2 we discuss evidence for ultrafast domain nucleation and percolation in literature and point out several correlated systems that can be potentially interesting for further ultrafast near-field investigation.

7.1. Mesoscopic physics in high T_c superconductors

Since the discovery of high-temperature superconductivity (HTSC) in 1986 [318], infrared studies have demonstrated time and again the ability to probe the essential characteristics of unconventional superconductors including the energy gap, pseudogap, and superfluid density [8]. More recently, these experiments have been extended to iron-based pnictide and chalcogenide materials [319–333]. Far-field IR spectroscopy, although an indirect probe, has revealed different types of intrinsic inhomogeneities in HTSC. For example: (1) A finite frequency peak at low energies is suggestive of impurities- or disorder-induced localization in $\text{YBa}_2(\text{Cu}_{1-x}\text{Zn}_x)_4\text{O}_8$ [334] and $\text{La}_{2-x}\text{Sr}_x\text{CuO}_4$ [335]; (2) Signatures in the spectral weight shift and mid-IR peaks can effectively probe charge and spin stripes in $\text{La}_{1.6-x}\text{Nd}_{0.4}\text{Sr}_x\text{CuO}_4$ [336], $\text{La}_{2-x}\text{Sr}_x\text{NiO}_4$ [337] and $\text{La}_{2-x}\text{Ba}_x\text{CuO}_4$ [338]; (3) In-plane anisotropic electromagnetic responses reveal striped order in $\text{YBa}_2\text{Cu}_3\text{O}_y$ and $\text{La}_{2-x}\text{Sr}_x\text{CuO}_4$ [335, 339], consistent with the notion of uni-directional stripe ordering; (4) Anomalous spectral weight shifts at IR and THz frequencies assigned to inhomogeneities of superfluid density [340].

In cuprates, various forms of CDWs were discovered to be strongly coupled to and compete with superconductivity in one of the cleanest HTSC compounds— $\text{YBa}_2\text{Cu}_3\text{O}_{6+y}$ (YBCO) [107, 122, 341–343], as schematically shown in figure 13(a) [314]. The spatial extent of the CDW-ordered regions can be rather large and reach micrometer sizes, as recently found in $\text{HgBa}_2\text{CuO}_{4+y}$ (figure 13(b)) [315]. These CDW-patches found in the CuO_2 plane are anti-correlated with the quenched disorder induced by oxygen-interstitial atomic stripes in the Hg–O plane and reveal a multi-scale nature of the phase inhomogeneities in layered cuprate compounds.

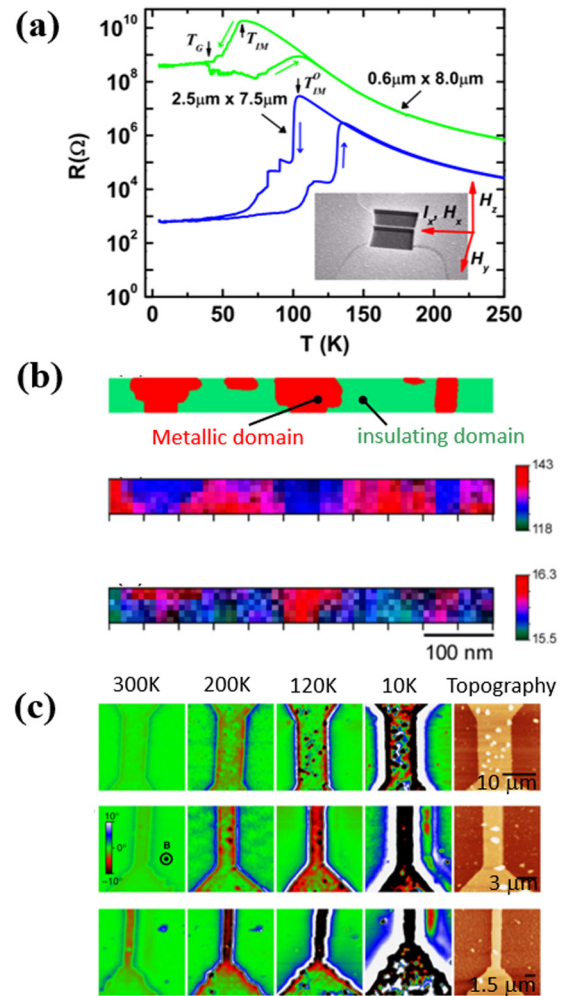


Figure 11. (a) Temperature dependent resistance for LPCMO bridges with two different widths [295]. Blue: $2.5 \mu\text{m}$ wide. Green: $0.6 \mu\text{m}$ wide. The step-like resistance change versus temperature is evident. The inset shows an SEM image of a $0.2 \mu\text{m}$ wide bridge with the orientations of applied magnetic fields H_x , H_y and H_z . (b) Metal–insulator phase separation in LPCMO nanowires at 150 K [296]. Top: schematic domain arrangement. Middle and bottom: cathode luminescence (CL) imaging with intensities integrated from 450 to 520 nm and 680 to 705 nm, respectively (c) temperature dependent MFM images of LPCMO under 9 T field [297]. The widths of the LPCMO stripes are 10 (top), 3 (middle) and 1.5 (bottom) μm . (a) Reproduced figure with permission from [295]. Copyright 2009 by the American Physical Society. (b) Reproduced figure with permission from [296]. Copyright 2015 by the American Chemical Society. (c) Reproduced by permission from Macmillan Publishers Ltd: [297], copyright 2015.

The phase diagram of iron-based superconductors such as $\text{Ca}(\text{Fe}_{1-x}\text{Co}_x)_2\text{As}_2$ reveals many similarities with the cuprates (figure 13(c)) [316]. Parent compounds are antiferromagnetic/orthorhombic phases where anisotropic nematic transport has been observed [109, 172–176, 178, 344]. IR spectroscopy when applied to untwinned samples of Fe-based materials, has emerged as a capable probe of the nematic state [345–348] through measurement with polarized light. The origin of nematicity is not firmly established [160]. Nematic fluctuations above the structural phase transition and the SC phase transition have been identified [174] near optimal doping. At

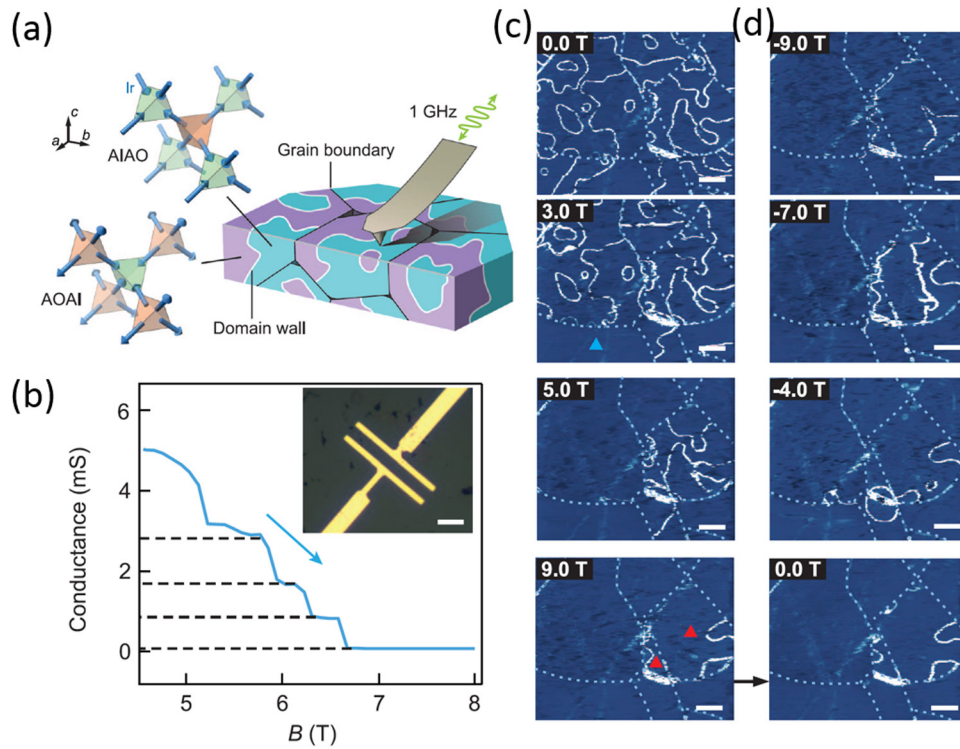


Figure 12. MIM study of pyrochlore $\text{Nd}_2\text{Ir}_2\text{O}_7$ domain walls. From [298]. Reprinted with permission from AAAS. (a) Left: schematics of all-in-all-out (AIAO) and all-out-all-in (AOAI) magnetic order. Right: schematics of domain walls and grain boundaries of a polished $\text{Nd}_2\text{Ir}_2\text{O}_7$ polycrystal surface under MIM investigation at 1 GHz. (b) Magnetic field dependent staircase-like conductance evolution measured by the electrodes (inset, scale bar: 5 μm). (c) MIM-Im images of field dependent domain wall evolution from 0 T to 9 T at 4.7 K. The blue triangle indicates the first grain to become a single domain. The red triangles mark the two grains that remain multidomain at 9 T. (d) The same region under investigation after the magnetic field sweeps back to 0 T (bottom) and then to -9 T (top). Scale bars in (c) and (d), 2 μm .

$T < T_c$, anisotropic energy gaps have been found in the SC state [6] and local measurements at the microscopic scale are shown to be of extreme importance [172, 349]. This is also the case in recently discovered $\text{A}_x\text{Fe}_{2-y}\text{Se}_2$ types of iron selenide compounds, where insulating regions and superconducting regions can coexist at mesoscopic scales, as revealed by a combination of high resolution STM measurement and a photoemission study of $\text{K}_2\text{Fe}_{2-y}\text{Se}_2$ [317] (figure 13(d)).

Figure 13 shows that micro-/mesoscopic separation of the superconducting and CDW/SDW/AF phases in cuprate and iron-based HTSC involves domain sizes from tens of nanometers to several microns. Therefore, nano-IR and nano-THz methods are potentially well suited to investigate micro- and mesoscopic correlated-electron phenomena in the HTSCs. Room temperature nano-IR measurements in $\text{Rb}_2\text{Fe}_4\text{Se}_5$ indeed revealed the phase segregation of AF and SC states with terraces perpendicular to the iron-selenide planes [350], in accord with the interesting physics suggested at interfaces [351–353]. Complex hierarchical 3D structures are also found in iron-selenide based HTSCs [354, 355] and reveal a highly organized percolating nature. Although cryogenic near-field data are not available to date, modeling predicts that s-SNOM at frequencies below the SC gap can have sufficient accuracy to probe the contrast between the normal and superconducting regions [252]. Moreover, low energy photons provide access to the superconducting energy gap in BCS superconductors and to the c -axis Josephson plasma frequency in the cuprates.

Due to the tip-induced finite momentum coupling in s-SNOM (section 3.2), it is also possible to excite and observe the dispersion of superfluid modes for prototypical high- T_c cuprates, as predicted by theoretical modeling of scanning plasmon interferometry [252]. Therefore, with future developments, s-SNOM imaging can shed new light on the nature of phase transitions HTSC systems, and specifically help us to understand the role of competing or coexisting ordered states near the superconducting transitions.

7.2. Dynamic phase separations in quantum materials

Phase separation is also relevant to the problems of the ultrafast nucleation and growth of photo-induced phases under fast excitations. Ultrafast optics serves as a capable tool to investigate quantum phenomena in correlated electron systems at fundamental time scales of the electron and lattice motion [11, 47, 50, 356, 357]. Previous work has shown that using optical-pump/optical-probe [29], optical-pump/THz-probe [38, 43, 358], and THz-pump/THz-probe techniques [42] one can gain significant insight into electron–electron and electron–lattice interactions in strongly correlated materials. The possibility to separate different degrees of freedom and observe the separation of electron or lattice domain growth has been suggested by several experiments. The dynamic far-infrared conductivity and lattice response induced by ultrafast optical pulses revealed essential inhomogeneities and domain expansion at the ultrafast time

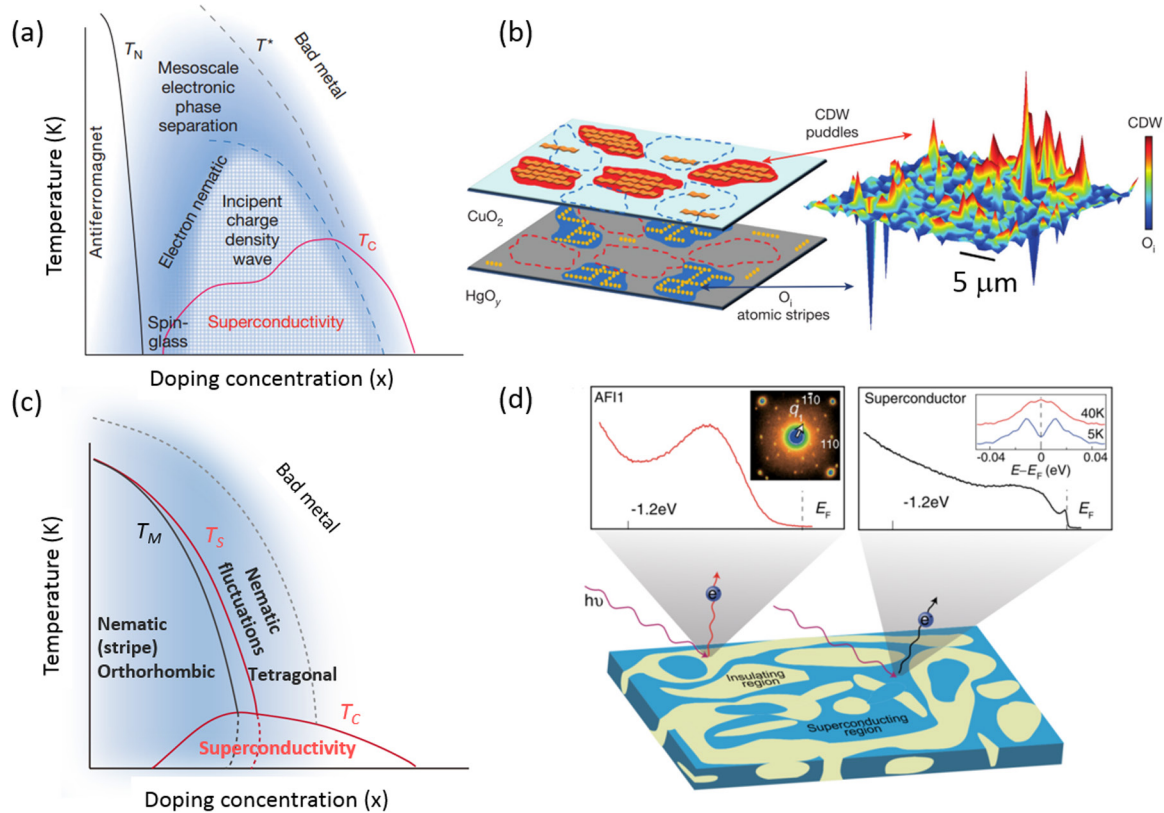


Figure 13. (a) Schematic phase diagram of cuprate HTSC (YBCO) as a function of temperature T and doping level x (oxygen content) [314] (b) schematic (left) and micro-x-ray diffraction imaging (right, difference map between the CDW-peak and oxygen-interstitial-streak intensity) of mesoscopic scale charge-density-wave puddles and quenched disorder in cuprate HTSC ($\text{HgBa}_2\text{CuO}_{4+y}$ (Hg1201)). Red puddles on the CuO_2 plane represent the CDW rich regions while blue areas on the Hg–O layers represent the oxygen-interstitial-rich regions [315]. (c) Schematic phase diagram of iron-based HTSC ($\text{Ca}(\text{Fe}_{1-x}\text{Co}_x)_2\text{As}_2$) with nematic electronic structure, recreated follow reference [316] (d) schematic phase separation of $\text{K}_x\text{Fe}_{2-y}\text{Se}_2$, the coexistence of AF insulating phases and SC phases yield a distribution of photoemission-spectroscopic signatures [317]. (a) Reproduced by permission from Macmillan Publishers Ltd: [314], copyright 2012. (b) Reproduced by permission from Macmillan Publishers Ltd: [315], copyright 2013. (c) Reproduced by permission from Macmillan Publishers Ltd: [316], copyright 2013. (d) Reproduced figure with permission from [317]. Copyright 2011 by the American Physical Society.

scale, indicating strong coupling between the electronic and lattice degrees of freedom, as demonstrated in several canonical transition metal oxides including Fe_3O_4 [359], V_2O_3 [360] and VO_2 [37, 39]. As ultrafast near-field nano-optical methods are becoming more and more adept in probing correlated materials, we anticipate these methods will play a significant role in the studies of new superconductors as well.

Fe_3O_4 is a mixed-valence oxide that undergoes a charge ordering transition (Verwey transition) from an electronically ordered insulator below ~ 120 K to a metal above [361]. Below 120 K, the distribution of the mixed-valence Fe^{3+} and Fe^{2+} is ordered in the form of linear three-Fe-site trimers ($\text{Fe}^{3+}\text{--}\text{Fe}^{2+}\text{--}\text{Fe}^{3+}$) [362]. The lattice structure also undergoes a phase transition from monoclinic to cubic at the transition temperature. With time-resolved x-ray diffraction and optical reflectivity measurements, de Jong *et al* demonstrated that photoexcitation at 800 nm can mobilize the three-Fe-site trimers across the insulator to metal transition and generate an inhomogeneous distribution of the trimeron annihilation [359]. This photo-induced transition can be divided into two stages. In the first stage, the ultrafast pump excitation generates holes in the quasi-static trimeron lattice at time < 300 fs. If the pump fluence is low, this initial photoexcited state simply returns to the monoclinic insulating phase with long-range

order through thermal equilibration. Above the pump fluence threshold (~ 1.3 mJ cm^{-2}), the initial dynamics are followed by a phase separated state with remnant trimeron patches rapidly shrinking at ~ 1.5 ps time scale, as clearly identified through the x-ray signatures of the electronic order.

The example in Fe_3O_4 revealed that threshold behavior and percolation processes determine time dynamics above 1 ps, which is roughly the upper limit of electron–phonon coupling time in correlated oxides. These dynamics can range from a few to tens of picoseconds, depending strongly on the initial temperature and fluence. Indeed, such an ultrafast percolative phase transition has also been suggested in an earlier optical pump THz probe study of VO_2 thin films and modeled using a Bruggeman effective medium theory (figure 14(a)) [39]. The dynamics can be intimately related to the local doping, defects and/or strain [37]. A more detailed analysis using scaling laws has recently been demonstrated in V_2O_3 using optical pump THz probe studies (figure 14(b)) [360]. Besides the anomalously long rise time, similar to that observed in Fe_3O_4 and VO_2 , a careful temperature and pump fluence dependent study of V_2O_3 reveals two prominent features in the ultrafast dynamics. The first is the delayed onset of the conductivity increase close to the zero time-delay. The second is the temperature and fluence dependent scaling of

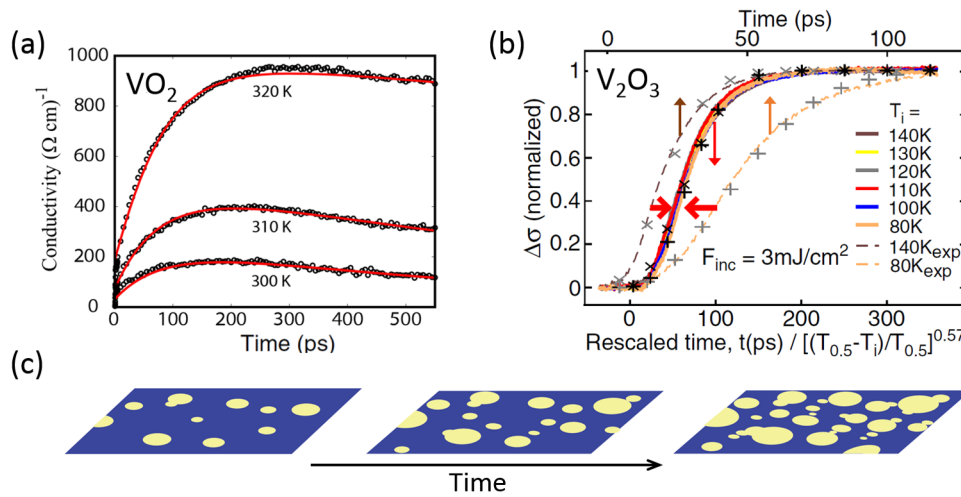


Figure 14. (a) Optical pump (800 nm) induced THz conductivity dynamics of a 100 nm VO_2 thin film on (100) MgO substrate [39]. Pump fluence: 12.8 mJ cm^{-2} (b) normalized optical pump (800 nm) induced THz conductivity dynamics of a 95 nm V_2O_3 thin film on (10 $\bar{1}$ 2) sapphire substrate [360]. Pump fluence: 3 mJ cm^{-2} ; T_i : initial temperature. The bottom (top) axis corresponds to the scaled (unscaled) data, shown by full (dashed) curves. (c) Schematics of 2D nucleation and growth of metallic domains (yellow regions) out of insulating background (purple region). Reproduced figure with permission from [360]. Copyright 2015 by the American Physical Society.

the dynamics. Pump probe traces that are taken at different initial temperatures with different pump fluences can be collapsed into a single curve with a renormalized time axis and a simple power law fit (figure 14(b)) [360]. This delayed rise time and universal scaling law arise from the spatial kinetics of the nucleation and growth of the metallic domains, where connections between measurements on the ultrafast timescale and classical models of nucleation and growth (Avrami equation) can be established.

The findings in ultrafast domain dynamics call for precise characterization of local material properties and domain growth following photo-excitation. The combination of the ultrafast and near-field techniques can in principle provide insight into the domain dynamics, as illustrated in figure 14(c). It would be also instructive to study the dynamical or persistent alternation of strain/lattice environment with photo-lattice control [30, 44, 45, 48, 363, 364] to manipulate material properties [30, 34, 42, 46, 48, 358, 365–368]. Phase inhomogeneity with simultaneous electric field gating [369–372] and photo excitation can be investigated in parallel as well. However, one has to keep in mind that, like any ‘far-field’ ultrafast experiments utilizing high repetition rate ultrafast lasers, contemporary ultrafast near-field methods probe averaged signals over numerous light pulses. A snapshot mapping of the domain growth dynamics of a single pulse induced spontaneous phase separation (without reproducible growth paths) is therefore demanding major breakthroughs in the field. The first strides have been reported in recent publications focused on VO_2 [56, 57].

8. Summary

In this Report, we have reviewed recent progress on near-field and microscopic characterization of quantum materials with strong electronic correlations. Still a nascent field, near-field nano-optics has already demonstrated an ability to investigate electronic, magnetic, and crystallographic textures that

are of quantum origin. We conclude by highlighting several important results and outline future instrumental innovations in nano-scopy tools motivated by the existing data:

- (1) The hierarchy of length scales in correlated quantum materials is fundamentally important for understanding the emergent complexities in this class of condensed matter systems;
- (2) Microscopic (and mesoscopic) textures and domain patterns vary with local strain environment and global symmetry of the dominant electronic and lattice states. Heterostructures and interfaces also exhibit unique and highly organized complex structures;
- (3) Future development of broadband near-field electromagnetic cryogenic imaging capabilities is needed for nanoscale spectroscopic characterizations of phase transitions in quantum materials that as a rule occur at low temperature. Examples include vanadium oxides, manganites, cuprates, iron-based HTSC and heavy fermion compounds. Ultrafast table-top lasers and synchrotron IR beamlines can serve as ideal broadband light sources for cryogenic s-SNOMs.
- (4) Spectroscopic investigations of collective electronic excitations such as plasmon and exciton modes in correlated systems have not been extensively studied. Tip-launched and/or tip-detected surface polaritonic propagation can be utilized to study light-matter interactions with high spatial resolution and high momentum coupling. Terahertz s-SNOM is an ideal technique for exploring nanoscale superfluid surface modes in superconductors.
- (5) A combination of femtosecond lasers and near-field optics will serve as a promising future direction of quantum materials research where ultrafast carrier- or lattice-dynamics can be understood with a microscopic perspective.
- (6) The combination of s-SNOM with a variety of scanning probe modes such as MFM, KPFM, and conducting AFM have not been explored extensively where a simultaneous monitoring of electronic, magnetic, and optical properties at local scale can be extremely interesting.

Acknowledgment

We would like to acknowledge Keji Lai, Stephanie Gilbert Corder, Aliaksei Charnukha, HT Stinson, Alex Frenzel, Alexander McLeod, Jamie Hinton and Xinzhong Chen for helpful discussions. Research in unconventional superconductivity and correlated oxides is supported by DE-SC0012375 and DE-SC0012592. Research on metal insulator transition is supported by ARO w911NF-13-1-0210. Development of nano-IR capabilities is supported by ARO w911NF-13-1-0210, AFOSR FA9550-15-1-0478 and ONR N00014-15-1-2671. DNB is the Moore Foundation Investigator in Quantum Materials, EPiQS Initiative GBMF4533.

References

- [1] Mott N F 1968 Metal–insulator transition *Rev. Mod. Phys.* **40** 677–83
- [2] Mathur N D and Littlewood P B 2003 Mesoscopic texture in manganites *Phys. Today* **56** 25
- [3] Dagotto E 2005 Complexity in strongly correlated electronic systems *Science* **309** 257–62
- [4] Kivelson S A *et al* 2003 How to detect fluctuating stripes in the high-temperature superconductors *Rev. Mod. Phys.* **75** 1201–41
- [5] Tranquada J M, Sternlieb B, Axe J and Nakamura Y 1995 Evidence for stripe correlations of spins and holes in copper oxide superconductors *Nature* **375** 561
- [6] Basov D N, Averitt R D, Van Der Marel D, Dressel M and Haule K 2011 Electrodynamics of correlated electron materials *Rev. Mod. Phys.* **83** 471–541
- [7] Armitage N P, Fournier P and Greene R L 2010 Progress and perspectives on electron-doped cuprates *Rev. Mod. Phys.* **82** 2421–87
- [8] Basov D and Timusk T 2005 Electrodynamics of high- T_c superconductors *Rev. Mod. Phys.* **77** 721–79
- [9] Miranda E and Dobrosavljevic V 2005 Disorder-driven non-Fermi liquid behavior of correlated electrons *Rep. Prog. Phys.* **68** 2337
- [10] Dagotto E 1994 Correlated electrons in high-temperature superconductors *Rev. Mod. Phys.* **66** 763–840
- [11] Orenstein J 2012 Ultrafast spectroscopy of quantum materials *Phys. Today* **65** 44–50
- [12] Tokura Y 2003 Correlated-electron physics in transition-metal oxides *Phys. Today* **56** 50–5
- [13] Imada M, Fujimori A and Tokura Y 1998 Metal–insulator transitions *Rev. Mod. Phys.* **70** 1039–263
- [14] Anderson P W 1972 More is different *Science* **177** 393–6
- [15] Demsar J, Averitt R D, Kabanov V V and Mihailovic D 2003 Photoinduced changes of reflectivity in single crystals of $\text{YBa}_2\text{Cu}_3\text{O}_{6.5}$ (ortho II) compound *Phys. Rev. Lett.* **91** 169701
- [16] Demsar J, Averitt R D and Taylor A J 2004 Nonequilibrium superconductivity probed by time-resolved far-infrared conductivity dynamics: comparison between MgB_2 and $\text{YBa}_2\text{Cu}_3\text{O}_7$ *J. Supercond.* **17** 143–9
- [17] Beyer M, Städter D, Beck M, Schäfer H, Kabanov V V, Logvenov G, Bozovic I, Koren G and Demsar J 2011 Photoinduced melting of superconductivity in the high- T_c superconductor $\text{La}_{2-x}\text{Sr}_x\text{CuO}_4$ probed by time-resolved optical and terahertz techniques *Phys. Rev. B* **83** 214515
- [18] Torchinsky D H, Mahmood F, Bollinger A T, Božović I and Gedik N 2013 Fluctuating charge-density waves in a cuprate superconductor *Nat. Mater.* **12** 387–91
- [19] Torchinsky D, Chen G, Luo J, Wang N and Gedik N 2010 Band-dependent quasiparticle dynamics in single crystals of the $\text{Ba}_{0.6}\text{K}_{0.4}\text{Fe}_2\text{As}_2$ superconductor revealed by pump-probe spectroscopy *Phys. Rev. Lett.* **105** 027005
- [20] Gedik N, Langner M, Orenstein J, Ono S, Abe Y and Ando Y 2005 Abrupt transition in quasiparticle dynamics at optimal doping in a cuprate superconductor system *Phys. Rev. Lett.* **95** 117005
- [21] Kabanov V V, Demsar J, Podobnik B and Mihailovic D 1999 Quasiparticle relaxation dynamics in superconductors with different gap structures: theory and experiments on $\text{YBa}_2\text{Cu}_3\text{O}_{7-D}$ *Phys. Rev. B* **59** 12
- [22] Kaiser S *et al* 2014 Optically induced coherent transport far above T_c in underdoped $\text{YBa}_2\text{Cu}_3\text{O}_{6+\delta}$ *Phys. Rev. B* **89** 184516
- [23] Buh J, Kabanov V, Baranov V, Mrzel A, Kovič A and Mihailovic D 2015 Control of switching between metastable superconducting states in δ -MoN nanowires *Nat. Commun.* **6** 10250
- [24] Madan I, Kurosawa T, Toda Y, Oda M, Mertelj T and Mihailovic D 2015 Evidence for carrier localization in the pseudogap state of cuprate superconductors from coherent quench experiments *Nat. Commun.* **6** 6958
- [25] Demsar J, Sarrao J L and Taylor A J 2006 Dynamics of photoexcited quasiparticles in heavy electron compounds *J. Phys.: Condens. Matter* **18** R281–314
- [26] Demsar J, Thorsmoelle V K, Sarrao J L and Taylor A J 2006 Photoexcited electron dynamics in Kondo insulators and heavy fermions *Phys. Rev. Lett.* **96** 37401
- [27] Demsar J, Averitt R D, Ahn K H, Graf M J, Trugman S A, Kabanov V V, Sarrao J L and Taylor A J 2003 Quasiparticle relaxation dynamics in heavy fermion compounds *Phys. Rev. Lett.* **91** 27401
- [28] Ahn K H, Graf M J, Trugman S A, Demsar J, Averitt R D, Sarrao J L and Taylor A J 2004 Ultrafast quasiparticle relaxation dynamics in normal metals and heavy-fermion materials *Phys. Rev. B* **69** 045114
- [29] Liu M K, Averitt R D, Durakiewicz T, Tobash P H, Bauer E D, Trugman S A, Taylor A J and Yarotski D A 2011 Evidence of a hidden-order pseudogap state in URu_2Si_2 using ultrafast optical spectroscopy *Phys. Rev. B* **84** 161101
- [30] Fausti D *et al* 2011 Light-induced superconductivity in a stripe-ordered cuprate *Science* **331** 189–91
- [31] Hu W *et al* 2014 Optically enhanced coherent transport in $\text{YBa}_2\text{Cu}_3\text{O}_{6.5}$ by ultrafast redistribution of interlayer coupling *Nat. Mater.* **13** 705–11
- [32] Cavalleri A, Toth C, Siders C W, Squier J A, Raksi F, Forget P and Kieffer J C 2001 Femtosecond structural dynamics in VO_2 during an ultrafast solid–solid phase transition *Phys. Rev. Lett.* **87** 237401
- [33] Morrison V R, Chatelain R P, Tiwari K L, Hendaoui A, Bruhacs A, Chaker M and Siwick B J 2014 A photoinduced metal-like phase of monoclinic VO_2 revealed by ultrafast electron diffraction *Science* **346** 445–8
- [34] Cavalleri A, Dekorsy T, Chong H, Kieffer J and Schoenlein R 2004 Evidence for a structurally-driven insulator-to-metal transition in VO_2 : a view from the ultrafast timescale *Phys. Rev. B* **70** 161102
- [35] Appavoo K, Wang B, Brady N F, Seo M, Nag J, Prasankumar R P, Hilton D J, Pantelides S T and Haglund R F 2014 Ultrafast phase transition via catastrophic phonon collapse driven by plasmonic hot-electron injection *Nano Lett.* **14** 1127–33
- [36] Rini M, Cavalleri A, Schoenlein R W, Lopez R, Feldman L C, Haglund R F Jr, Boatner L A and Haynes T E 2005 Photoinduced phase transition in VO_2 nanocrystals. Ultrafast control of surface-plasmon resonance *Opt. Lett.* **30** 558–60

- [37] O'Callahan B T, Jones A C, Hyung Park J, Cobden D H, Atkin J M and Raschke M B 2015 Inhomogeneity of the ultrafast insulator-to-metal transition dynamics of VO₂ *Nat. Commun.* **6** 6849
- [38] Kübler C *et al* 2007 Coherent structural dynamics and electronic correlations during an ultrafast insulator–metal phase transition in VO₂ *Phys. Rev. Lett.* **99** 116401
- [39] Hilton D J *et al* 2007 Enhanced photosusceptibility near T_c for the light-induced insulator-to-metal phase transition in vanadium dioxide *Phys. Rev. Lett.* **99** 226401
- [40] Cocker T L, Titova L V, Fourmaux S, Holloway G, Bandulet H-C, Brassard D, Kieffer J-C, El Khakani M A and Hegmann F A 2012 Phase diagram of the ultrafast photoinduced insulator–metal transition in vanadium dioxide *Phys. Rev. B* **85** 155120
- [41] Liu M, Ji N, Lin Z and Chui S T 2005 Radiation torque on a birefringent sphere caused by an electromagnetic wave *Phys. Rev. E* **72** 056610
- [42] Liu M *et al* 2012 Terahertz-field-induced insulator-to-metal transition in vanadium dioxide metamaterial *Nature* **487** 345–8
- [43] Pashkin A, Kübler C, Ehrke H, Lopez R, Halabica A, Haglund R F, Huber R and Leitenstorfer A 2011 Ultrafast insulator–metal phase transition in VO₂ studied by multiterahertz spectroscopy *Phys. Rev. B* **83** 195120
- [44] Caviglia A *et al* 2012 Ultrafast strain engineering in complex oxide heterostructures *Phys. Rev. Lett.* **108** 136801
- [45] Först M *et al* 2011 Driving magnetic order in a manganite by ultrafast lattice excitation *Phys. Rev. B* **84** 241104(R)
- [46] Fiebig M, Miyano K, Tomioka Y and Tokura Y 2000 Sub-picosecond photo-induced melting of a charge-ordered state in a perovskite manganite *Appl. Phys. B* **71** 211–5
- [47] Averitt R D and Taylor A J 2002 Ultrafast optical and far-infrared quasiparticle dynamics in correlated electron materials *J. Phys.: Condens. Matter* **14** R1357–90
- [48] Rini M, Tobey R, Dean N, Itatani J, Tomioka Y, Tokura Y, Schoenlein R W and Cavalleri A 2007 Control of the electronic phase of a manganite by mode-selective vibrational excitation *Nature* **449** 72–4
- [49] Averitt R D, Lobad A I, Kwon C, Trugman S A, Thorsmolle V K and Taylor A J 2001 Ultrafast conductivity dynamics in colossal magnetoresistance manganites *Phys. Rev. Lett.* **87** 17401
- [50] Ichikawa H *et al* 2011 Transient photoinduced ‘hidden’ phase in a manganite *Nat. Mater.* **10** 101–5
- [51] Zhang J and Averitt R D 2014 Dynamics and control in complex transition metal oxides *Annu. Rev. Mater. Res.* **44** 19–43
- [52] Vaskivskiy I, Gospodaric J, Brazovskii S, Svetin D, Sutar P, Goreshnik E, Mihailovic I A, Mertelj T and Mihailovic D 2015 Controlling the metal-to-insulator relaxation of the metastable hidden quantum state in 1T-TaS₂ *Sci. Adv.* **1** e1500168
- [53] Wagner M *et al* 2014 Ultrafast and nanoscale plasmonic phenomena in exfoliated graphene revealed by infrared pump-probe nanoscopy *Nano Lett.* **14** 894–900
- [54] Wagner M *et al* 2014 Ultrafast dynamics of surface plasmons in InAs by time-resolved infrared nanospectroscopy *Nano Lett.* **14** 4529–34
- [55] Eisele M, Cocker T L, Huber M A, Plankl M, Viti L, Ercolani D, Sorba L, Vitiello M S and Huber R 2014 Ultrafast multi-terahertz nano-spectroscopy with sub-cycle temporal resolution *Nat. Photon.* **8** 841
- [56] Huber M A *et al* 2016 Ultrafast mid-infrared nanoscopy of strained vanadium dioxide nanobeams *Nano Lett.* **16** 1421–7
- [57] Dönges S A, Khatib O, O'Callahan B T, Atkin J M, Park J H, Cobden D and Raschke M B 2016 Ultrafast nanoimaging of the photoinduced phase transition dynamics in VO₂ *Nano Lett.* **16** 3029
- [58] Ni G X *et al* 2016 Ultrafast optical switching of infrared plasmon polaritons in high-mobility graphene *Nat. Photon.* **10** 244–8
- [59] Kuschewski F, Kehr S C, Green B, Bauer C, Gensch M and Eng L M 2015 Optical nanoscopy of transient states in condensed matter *Sci. Rep.* **5** 12582
- [60] Pohl D W, Denk W and Lanz M 1984 Optical stethoscopy: image recording with resolution $\lambda/20$ *Appl. Phys. Lett.* **44** 651
- [61] Lewis A, Isaacson M, Harootunian A and Muray A 1984 Development of a 500 Å spatial resolution light microscope *Ultramicroscopy* **13** 227–31
- [62] Inoué Y and Kawata S 1994 Near-field scanning optical microscope with a metallic probe tip *Opt. Lett.* **19** 159
- [63] Specht M, Pedarnig J and Heckl W 1992 Scanning plasmon near-field microscope *Phys. Rev. Lett.* **68** 476
- [64] Wessel J 1985 Surface-enhanced optical microscopy *J. Opt. Soc. Am. B* **2** 1538
- [65] Betzig E, Trautman J K, Harris T D, Weiner J S and Kostelak R L 1991 Breaking the diffraction barrier: optical microscopy on a nanometric scale *Science* **251** 1468–70
- [66] Knoll B and Keilmann F 1999 Near-field probing of vibrational absorption for chemical microscopy *Nature* **399** 134–7
- [67] Novotny L 2008 The history of near-field optics *Prog. Opt.* **50** 137–84
- [68] Qazilbash M M *et al* 2007 Mott transition in VO₂ revealed by infrared spectroscopy and nano-imaging *Science* **318** 1750–3
- [69] Alonso-Gonzalez P *et al* 2014 Controlling graphene plasmons with resonant metal antennas and spatial conductivity patterns *Science* **344** 1369–73
- [70] Chen J *et al* 2012 Optical nano-imaging of gate-tunable graphene plasmons *Nature* **487** 77
- [71] Woessner A *et al* 2014 Highly confined low-loss plasmons in graphene–boron nitride heterostructures *Nat. Mater.* **14** 421–5
- [72] Yoxall E *et al* 2015 Direct observation of ultraslow hyperbolic polariton propagation with negative phase velocity *Nat. Photon.* **9** 674–9
- [73] Dai S *et al* 2015 Subdiffractional focusing and guiding of polaritonic rays in a natural hyperbolic material *Nat. Commun.* **6** 6963
- [74] Fei Z *et al* 2013 Electronic and plasmonic phenomena at graphene grain boundaries *Nat. Nanotechnol.* **8** 821–5
- [75] Dai S *et al* 2015 Graphene on hexagonal boron nitride as a tunable hyperbolic metamaterial *Nat. Nanotechnol.* **10** 682
- [76] Fei Z *et al* 2012 Gate-tuning of graphene plasmons revealed by infrared nano-imaging *Nature* **487** 82
- [77] Ni G X *et al* 2015 Plasmons in graphene moiré superlattices *Nat. Mater.* **14** 1217
- [78] Fei Z *et al* 2015 Tunneling plasmonics in bilayer graphene *Nano Lett.* **15** 4973
- [79] Basov D N, Fogler M M, Lanzara A, Wang F and Zhang Y 2014 Colloquium: graphene spectroscopy *Rev. Mod. Phys.* **86** 959–94
- [80] Fei Z *et al* 2015 Edge and surface plasmons in graphene nanoribbons *Nano Lett.* **15** 8271–6
- [81] O'Callahan B T, Lewis W E, Jones A C and Raschke M B 2014 Spectral frustration and spatial coherence in thermal near-field spectroscopy *Phys. Rev. B* **89** 245446
- [82] Jones A C, O'Callahan B T, Yang H U and Raschke M B 2013 The thermal near-field: coherence, spectroscopy, heat-transfer, and optical forces *Prog. Surf. Sci.* **88** 349–92
- [83] Woessner A *et al* 2016 Near-field photocurrent nanoscopy on bare and encapsulated graphene *Nat. Commun.* **7** 10783

- [84] Fisher B 1975 Moving boundaries and travelling domains during switching of VO₂ single crystals *J. Phys. C: Solid State Phys.* **8** 2072
- [85] He X *et al* 2014 *In situ* atom scale visualization of domain wall dynamics in VO₂ insulator–metal phase transition *Sci. Rep.* **4** 6544
- [86] Liu M *et al* 2015 Phase transition in bulk single crystals and thin films of VO₂ by nanoscale infrared spectroscopy and imaging and spectroscopy *Phys. Rev. B* **91** 245155
- [87] Lupi S *et al* 2010 A microscopic view on the mott transition in chromium-doped V₂O₃ *Nat. Commun.* **1** 105
- [88] Liu M K *et al* 2013 Anisotropic electronic state via spontaneous phase separation in strained vanadium dioxide films *Phys. Rev. Lett.* **111** 096602
- [89] Liu M *et al* 2014 Symmetry breaking and geometric confinement in VO₂: results from a three-dimensional infrared nano-imaging *Appl. Phys. Lett.* **104** 121905
- [90] Tselev A, Meunier V, Strelcov E, Shelton W A, Luk'yanchuk I A, Jones K, Proksch R, Kolmakov A and Kalinin S V 2010 Mesoscopic metal–insulator transition at ferroelastic domain walls in VO₂ *ACS Nano* **4** 4412–9
- [91] Tselev A *et al* 2010 Interplay between ferroelastic and metal–insulator phase transitions in strained quasi-two-dimensional VO₂ nanoplatelets *Nano Lett.* **10** 2003–11
- [92] Strelcov E, Tselev A, Ivanov I, Budai J D, Zhang J, Tischler J Z, Kravchenko I, Kalinin S V and Kolmakov A 2012 Doping-based stabilization of the M2 phase in free-standing VO₂ nanostructures at room temperature *Nano Lett.* **12** 6198–205
- [93] Fan W, Huang S, Cao J, Ertekin E, Barrett C, Khanal D R, Grossman J C and Wu J 2009 Superelastic metal–insulator phase transition in single-crystal VO₂ nanobeams *Phys. Rev. B* **80** 241105
- [94] Xie R, Bui C T, Varghese B, Zhang Q, Sow C H, Li B and Thong J T L 2011 An electrically tuned solid-state thermal memory based on metal–insulator transition of single-crystalline VO₂ nanobeams *Adv. Funct. Mater.* **21** 1602–7
- [95] Wu J, Gu Q, Guiton B S, De Leon N P, Ouyang L and Park H 2006 Strain-induced self organization of metal–insulator domains in single-crystalline VO₂ nanobeams *Nano Lett.* **6** 2313–7
- [96] Hu B, Ding Y, Chen W, Kulkarni D, Shen Y, Tsukruk V V and Wang Z L 2010 External-strain induced insulating phase transition in VO₂ nanobeam and its application as flexible strain sensor *Adv. Mater.* **22** 5134–9
- [97] Zhang S, Chou J Y and Lauhon L J 2009 Direct correlation of structural domain formation with the metal insulator transition in a VO₂ nanobeam *Nano Lett.* **9** 4527–32
- [98] Cao J *et al* 2010 Extended mapping and exploration of the vanadium dioxide stress-temperature phase diagram *Nano Lett.* **10** 2667–73
- [99] Cao J and Wu J 2011 Strain effects in low-dimensional transition metal oxides *Mater. Sci. Eng. R* **71** 35–52
- [100] Jones A C, Berweger S, Wei J, Cobden D and Raschke M B 2010 Nano-optical investigations of the metal–insulator phase behavior of individual VO₂ microcrystals *Nano Lett.* **10** 1574–81
- [101] Atkin J M, Berweger S, Jones A C and Raschke M B 2014 Nano-optical imaging and spectroscopy of order, phases, and domains in complex solids *Adv. Phys.* **61** 745–842
- [102] Atkin J, Berweger S, Chavez E, Raschke M, Cao J, Fan W and Wu J 2012 Strain and temperature dependence of the insulating phases of VO₂ near the metal–insulator transition *Phys. Rev. B* **85** 020101
- [103] Ma E Y, Bryant B, Tokunaga Y, Aeppli G, Tokura Y and Shen Z-X 2015 Charge-order domain walls with enhanced conductivity in a layered manganite *Nat. Commun.* **6** 7595
- [104] Akahoshi D, Uchida M, Tomioka Y, Arima T, Matsui Y and Tokura Y 2003 Random potential effect near the bicritical region in perovskite manganites as revealed by comparison with the ordered perovskite analogs *Phys. Rev. Lett.* **90** 177203
- [105] Wu W, Israel C, Hur N, Park S, Cheong S-W and de Lozanne A 2006 Magnetic imaging of a supercooling glass transition in a weakly disordered ferromagnet *Nat. Mater.* **5** 881–6
- [106] Burkhardt M H *et al* 2012 Imaging the first-order magnetic transition in La_{0.35}Pr_{0.275}Ca_{0.375}MnO₃ *Phys. Rev. Lett.* **108** 1–5
- [107] Chang J *et al* 2012 Direct observation of competition between superconductivity and charge density wave order in YBa₂Cu₃O_{6.67} *Nat. Phys.* **8** 871–6
- [108] Mross D F and Senthil T 2012 Stripe melting and quantum criticality in correlated metals *Phys. Rev. B* **86** 115138
- [109] Chuang T-M, Allan M P, Lee J, Xie Y, Ni N, Bud'ko S L, Boebinger G S, Canfield P C and Davis J C 2010 Nematic electronic structure in the 'parent' state of the iron-based superconductor Ca(Fe(1 - x)Co(x))₂As₂ *Science* **327** 181–4
- [110] Nie L, Tarjus G and Kivelson S A 2014 Quenched disorder and vestigial nematicity in the pseudo-gap regime of the cuprates *PNAS* **111** 7980
- [111] Machida T, Fujisawa Y, Nagao M, Demura S, Deguchi K, Mizuguchi Y, Takano Y and Sakata H 2014 Checkerboard stripe electronic state on cleaved surface of NdO_{0.7}F_{0.3}BiS₂ probed by scanning tunneling microscopy *J. Phys. Soc. Japan* **83** 113701
- [112] Wise W D, Boyer M C, Chatterjee K, Kondo T, Takeuchi T, Ikuta H, Wang Y Y and Hudson E W 2008 Charge-density-wave origin of cuprate checkerboard visualized by scanning tunnelling microscopy *Nat. Phys.* **4** 696
- [113] Blatter G, Feigel'man M V, Geshkenbein V B, Larkin A I and Vinokur V M 1994 Vortices in high-temperature superconductors *Rev. Mod. Phys.* **66** 1125–388
- [114] Kontos T, Aprili M, Lesueur J and Grison X 2001 Inhomogeneous superconductivity induced in a ferromagnet by proximity effect *Phys. Rev. Lett.* **86** 304–7
- [115] Seo S *et al* 2014 Disorder in quantum critical superconductors *Nat. Phys.* **10** 120
- [116] Hamidian M H *et al* 2011 How Kondo-holes create intense nanoscale heavy-fermion hybridization disorder *Proc. Natl Acad. Sci.* **108** 18233–7
- [117] Bauer E D *et al* 2011 Electronic inhomogeneity in a Kondo lattice *Proc. Natl Acad. Sci.* **108** 6857–61
- [118] Dagotto E, Hotta T and Moreo A 2001 Colossal magnetoresistant materials: the key role of phase separation *Phys. Rep.* **344** 1–153
- [119] Moreo A, Mayr M, Feiguin A, Yunoki S and Dagotto E 2000 Giant cluster coexistence in doped manganites and other compounds *Phys. Rev. Lett.* **84** 5568–71
- [120] Robertson J A, Kivelson S A, Fradkin E, Fang A C and Kapitulnik A 2006 Distinguishing patterns of charge order: stripes or checkerboards *Phys. Rev. B* **74** 134507
- [121] Del Maestro A, Rosenow B and Sachdev S 2006 From stripe to checkerboard ordering of charge-density waves on the square lattice in the presence of quenched disorder *Phys. Rev. B* **74** 024520
- [122] Achkar A J, Mao X, McMahon C, Sutarto R, He F, Liang R, Bonn D A, Hardy W N and Hawthorn D G 2014 Impact of quenched oxygen disorder on charge density wave order in YBa₂Cu₃O_{6+x} *Phys. Rev. Lett.* **113** 107002
- [123] Lorenzana J, Castellani C and Di Castro C 2002 Mesoscopic frustrated phase separation in electronic systems *Europhys. Lett.* **57** 704–10
- [124] Jamei R, Kivelson S and Spivak B 2005 Universal aspects of coulomb-frustrated phase separation *Phys. Rev. Lett.* **94** 1–5

- [125] Chen C and Cheong S-W 1996 Commensurate to incommensurate charge ordering and its real-space images in $\text{La}_{0.5}\text{Ca}_{0.5}\text{MnO}_3$ *Phys. Rev. Lett.* **76** 4042–5
- [126] Mori S, Chen C and Cheong S 1998 Pairing of charge-ordered stripes in $(\text{La}, \text{Ca})\text{MnO}_3$ *Nature* **392** 473–6
- [127] Loudon J C, Cox S, Williams A J, Attfield J P, Littlewood P B, Midgley P A and Mathur N D 2005 Weak charge-lattice coupling requires reinterpretation of stripes of charge order in $\text{La}_{1-x}\text{Ca}_x\text{MnO}_3$ *Phys. Rev. Lett.* **94** 5–8
- [128] Parker C V, Aynajian P, da Silva Neto E H, Pushp A, Ono S, Wen J, Xu Z, Gu G and Yazdani A 2010 Fluctuating stripes at the onset of the pseudogap in the high- T_c superconductor $\text{Bi}_2\text{Sr}_2\text{CaCu}_2\text{O}_{8+x}$ *Nature* **468** 677–80
- [129] Tranquada J M, Axe J D, Ichikawa N, Moodenbaugh A R, Nakamura Y and Uchida S 1996 Coexistence of, and competition between, superconductivity and charge-stripe order in $\text{La}(1.6-x)\text{Nd}(0.4)\text{Sr}(x)\text{CuO}(4)$ *Phys. Rev. Lett.* **78** 338
- [130] Vojta M and Sachdev S 1999 Charge order, superconductivity, and a global phase diagram of doped antiferromagnets *Phys. Rev. Lett.* **83** 3916
- [131] McElroy K, Lee D-H, Hoffman J E, Lang K M, Lee J, Hudson E W, Eisaki H, Uchida S and Davis J C 2005 Coincidence of checkerboard charge order and antinodal state decoherence in strongly underdoped superconducting $\text{Bi}_2\text{Sr}_2\text{CaCu}_2\text{O}_{8+\delta}$ *Phys. Rev. Lett.* **94** 197005
- [132] Castro Neto A H 2001 Charge density wave, superconductivity, and anomalous metallic behavior in 2D transition metal dichalcogenides *Phys. Rev. Lett.* **86** 4382–5
- [133] McMillan W 1976 Theory of discommensurations and the commensurate-incommensurate charge-density-wave phase transition *Phys. Rev. B* **14** 1496–502
- [134] Carpinelli J M, Weitering H H, Plummer E W and Stumpf R 1996 Direct observation of a surface charge density wave *Nature* **381** 398
- [135] Hirsch J E 1984 Charge-density-wave to spin-density-wave transition in the extended Hubbard model *Phys. Rev. Lett.* **53** 2327
- [136] Grüner G 1988 The dynamics of charge-density waves *Rev. Mod. Phys.* **60** 1129–81
- [137] Littlewood P B and Varma C M 1982 Amplitude collective modes in superconductors and their coupling to charge-density waves *Phys. Rev. B* **26** 4883–93
- [138] Daemen L L and Overhauser A W 1989 Superconductivity and charge-density waves *Phys. Rev. B* **40** 124–8
- [139] Homes C C, Dordevic S V, Gu G D, Li Q, Valla T and Tranquada J M 2006 Charge order, metallic behavior, and superconductivity in $\text{La}_{2-x}\text{Ba}_x\text{CuO}_4$ with $x = 1/8$ *Phys. Rev. Lett.* **96** 257002
- [140] Stewart G R 1984 Heavy-fermion systems *Rev. Mod. Phys.* **56** 755–87
- [141] Fradkin E, Kivelson S A and Tranquada J M 2015 Colloquium: theory of intertwined orders in high temperature superconductors *Rev. Mod. Phys.* **87** 457–82
- [142] Kim K W, Pashkin A, Schäfer H, Beyer M, Porer M, Wolf T, Bernhard C, Demsar J, Huber R and Leitenstorfer A 2012 Ultrafast transient generation of spin-density-wave order in the normal state of $\text{BaFe}(\text{2})\text{As}(\text{2})$ driven by coherent lattice vibrations *Nat. Mater.* **11** 497–501
- [143] Chen H 2009 Coexistence of the spin-density wave and superconductivity *Coexistence* **17006** 1–6
- [144] Chen H-D, Vafeek O, Yazdani A and Zhang S-C 2004 Pair density wave in the pseudogap state of high temperature superconductors *Phys. Rev. Lett.* **93** 187002
- [145] Cho G Y, Soto-Garrido R and Fradkin E 2014 Topological pair-density-wave superconducting states *Phys. Rev. Lett.* **113** 256405
- [146] Berg E, Fradkin E and Kivelson S A 2010 Pair-density-wave correlations in the Kondo–Heisenberg model *Phys. Rev. Lett.* **105** 146403
- [147] Berg E, Fradkin E and Kivelson S A 2009 Charge $-4e$ superconductivity from pair density wave order in certain high temperature superconductors *Nat. Phys.* **5** 830
- [148] Agterberg D F and Tsunetsugu H 2008 Dislocations and vortices in pair density wave superconductors *Nat. Phys.* **4** 639
- [149] Nayak C 2000 Density-wave states of nonzero angular momentum *Phys. Rev. B* **62** 4880–9
- [150] Zhu J-X, Kim W, Ting C S and Carbotte J P 2001 Quasiparticle states around a nonmagnetic impurity in a d-density-wave state of high- T_c cuprates *Phys. Rev. Lett.* **87** 197001
- [151] Wang Q-H, Han J H and Lee D-H 2001 Superfluid density in the d-density-wave scenario *Phys. Rev. Lett.* **87** 077004
- [152] Chakravarty S, Kee H-Y and Nayak C 2001 Neutron scattering signature of d-density wave order in the cuprates *Int. J. Mod. Phys. B* **15** 2901–9
- [153] Tewari S, Kee H-Y, Nayak C and Chakravarty S 2001 Spin and current correlation functions in the d-density-wave state of the cuprates *Phys. Rev. B* **64** 224516
- [154] Chakravarty S, Laughlin R B, Morr D K and Nayak C 2001 Hidden order in the cuprates *Phys. Rev. B* **63** 094503
- [155] Nguyen H and Chakravarty S 2002 Effects of magnetic field on the d-density-wave order in the cuprates *Phys. Rev. B* **65** 180519
- [156] Chakravarty S, Nayak C and Tewari S 2003 Angle-resolved photoemission spectra in the cuprates from the d-density wave theory *Phys. Rev. B* **68** 100504(R)
- [157] Oganesyan V and Ussishkin I 2004 Nernst effect, quasiparticles, and d-density waves in cuprates *Phys. Rev. B* **70** 054503
- [158] Abbamonte P, Rusydi A, Smadici S, Gu G D, Sawatzky G A and Feng D L 2005 Spatially modulated ‘mottness’ in $\text{La}_{2-x}\text{Ba}_x\text{CuO}_4$ *Nat. Phys.* **1** 155–8
- [159] Phillabaum B and Carlson E 2008 Harmonic peaks of stripe phases in cuprates *Phys. Rev. B* **77** 104526
- [160] Fernandes R M, Chubukov A V and Schmalian J 2014 What drives nematic order in iron-based superconductors? *Nat. Phys.* **10** 97–104
- [161] Ando Y, Segawa K, Komiya S and Lavrov A N 2002 Electrical resistivity anisotropy from self-organized one dimensionality in high-temperature superconductors *Phys. Rev. Lett.* **88** 137005
- [162] Howald C, Eisaki H, Kaneko N, Greven M and Kapitulnik A 2003 Periodic density-of-states modulations in superconducting $\text{Bi}_2\text{Sr}_2\text{CaCu}_2\text{O}_{8+\delta}$ *Phys. Rev. B* **67** 014533
- [163] Xia J *et al* 2008 Polar Kerr-effect measurements of the high-temperature $\text{YBa}_2\text{Cu}_3\text{O}_{6+x}$ superconductor: evidence for broken symmetry near the pseudogap temperature *Phys. Rev. Lett.* **100** 127002
- [164] Hinkov V, Haug D, Fauqué B, Bourges P, Sidis Y, Ivanov A, Bernhard C, Lin C T and Keimer B 2008 Electronic liquid crystal state in the high-temperature superconductor $\text{YBa}_2\text{Cu}_3\text{O}_{6.45}$ *Science* **319** 597–601
- [165] Fradkin E, Kivelson S A, Lawler M J, Eisenstein J P and Mackenzie A P 2010 Nematic fermi fluids in condensed matter physics *Annu. Rev. Condens. Matter Phys.* **1** 153–78
- [166] Daou R *et al* 2010 Broken rotational symmetry in the pseudogap phase of a high- T_c superconductor *Nature* **463** 519–22
- [167] Lawler M J *et al* 2010 Intra-unit-cell electronic nematicity of the high- T_c copper-oxide pseudogap states *Nature* **466** 347–51

- [168] Grissonnanche G *et al* 2014 Direct measurement of the upper critical field in cuprate superconductors *Nat. Commun.* **5** 3280
- [169] Fujita K *et al* 2014 Simultaneous transitions in cuprate *Science* **344** 612–6
- [170] Wu T, Mayaffre H, Krämer S, Horvatić M, Berthier C, Hardy W N, Liang R, Bonn D A and Julien M-H 2015 Incipient charge order observed by NMR in the normal state of $\text{YBa}_2\text{Cu}_3\text{O}_y$ *Nat. Commun.* **6** 6438
- [171] Phillabaum B, Carlson E W and Dahmen K A 2012 Spatial complexity due to bulk electronic nematicity in a superconducting underdoped cuprate *Nat. Commun.* **3** 915
- [172] Chu J-H *et al* 2010 In-plane resistivity anisotropy in an underdoped iron arsenide superconductor *Science* **329** 824–6
- [173] Fernandes R M *et al* 2010 Effects of nematic fluctuations on the elastic properties of iron arsenide superconductors *Phys. Rev. Lett.* **105** 157003
- [174] Kasahara S *et al* 2012 Electronic nematicity above the structural and superconducting transition in $\text{BaFe}_2(\text{As}_{1-x}\text{P}_x)_2$ *Nature* **486** 382–5
- [175] Chu J-H, Kuo H-H, Analytis J G and Fisher I R 2012 Divergent nematic susceptibility in an iron arsenide superconductor *Science* **337** 710–2
- [176] Yoshizawa M *et al* 2012 Structural quantum criticality and superconductivity in iron-based superconductor $\text{Ba}(\text{Fe}_{1-x}\text{Co}_x)_2\text{As}_2$ *J. Phys. Soc. Japan* **81** 024604
- [177] Gallais Y *et al* 2013 Observation of incipient charge nematicity in $\text{Ba}(\text{Fe}_{1-x}\text{Co}_x)_2\text{As}_2$ *Phys. Rev. Lett.* **111** 267001
- [178] Rosenthal E P *et al* 2014 Visualization of electron nematicity and unidirectional antiferroic fluctuations at high temperatures in NaFeAs *Nat. Phys.* **10** 225–32
- [179] Maier T A and Scalapino D J 2014 Pairing interaction near a nematic quantum critical point of a three-band CuO_2 model *Phys. Rev. B* **90** 174510
- [180] Lederer S, Schattner Y, Berg E and Kivelson S A 2015 Enhancement of superconductivity near a nematic quantum critical point *Phys. Rev. Lett.* **114** 097001
- [181] Binder K 1987 Theory of first-order phase transitions *Rep. Prog. Phys.* **50** 783
- [182] Uemura Y J *et al* 2006 Phase separation and suppression of critical dynamics at quantum phase transitions of MnSi and $(\text{Sr}_{1-x}\text{Ca}_x)\text{RuO}_3$ *Nat. Phys.* **3** 29–35
- [183] Ward T Z, Gai Z, Guo H W, Yin L F and Shen J 2011 Dynamics of a first-order electronic phase transition in manganites *Phys. Rev. B* **83** 125125
- [184] Khomskii D I 2014 *Transition Metal Compounds* (Cambridge: Cambridge University Press)
- [185] Uehara M, Mori S, Chen C H and Cheong S-W 1999 Percolative phase separation underlies colossal magnetoresistance in mixed-valent manganites *Nature* **399** 560–3
- [186] Hehn M, Ounadjela K, Bucher J-P, Rousseaux F, Decanini D, Bartenlian B and Chappert C 1996 Nanoscale magnetic domains in mesoscopic magnets *Science* **272** 1782–5
- [187] Moreo A, Yunoki S and Dagotto E 1999 Phase separation scenario for manganese oxides and related materials *Science* **283** 2034–40
- [188] Wu T *et al* 2001 Electroresistance and electronic phase separation in mixed-valent manganites *Phys. Rev. Lett.* **86** 5998–6001
- [189] Dagotto E 2002 *Nanoscale Phase Separation and Colossal Magnetoresistance* (Berlin: Springer)
- [190] Ahn K, Lookman T and Bishop A 2004 Strain-induced metal–insulator phase coexistence in perovskite manganites *Nature* **428** 401–4
- [191] Lai K, Nakamura M, Kundhikanjana W, Kawasaki M, Tokura Y, Kelly M A and Shen Z-X 2010 Mesoscopic percolating resistance network in a strained manganite thin film *Science* **329** 190–3
- [192] Jeon H and Biswas A 2010 Single domain to multi-domain transition due to in-plane magnetic anisotropy in phase separated $(\text{La}_{0.4}\text{Pr}_{0.6})_{0.67}\text{Ca}_{0.33}\text{O}_3$ thin films *Phys. Rev. B* **83** 064408
- [193] Mishra D K, Sathe V G, Rawat R, Ganesan V, Kumar R and Sharma T K 2015 Controlling phase separation in $\text{La}_{5/8-y}\text{Pr}_y\text{Ca}_{3/8}\text{MnO}_3$ ($y = 0.45$) epitaxial thin films by strain disorder *Appl. Phys. Lett.* **106** 072401
- [194] Koulakov A A, Fogler M M and Shklovskii B I 1996 Charge density wave in two-dimensional electron liquid in weak magnetic field *Phys. Rev. Lett.* **76** 499–502
- [195] High A A, Leonard J R, Hammack A T, Fogler M M, Butov L V, Kavokin A V, Campman K L and Gossard A C 2012 Spontaneous coherence in a cold exciton gas *Nature* **483** 584–8
- [196] Shenoy V B, Sarma D D and Rao C N R 2006 Electronic phase separation in correlated oxides: the phenomenon, its present status and future prospects *ChemPhysChem* **7** 2053–9
- [197] Kivelson S A, Fradkin E and Emery V J 1998 Electronic liquid-crystal phases of a doped mott insulator *Nature* **393** 550–3
- [198] Carlson E W and Dahmen K A 2011 Using disorder to detect locally ordered electron nematics via hysteresis *Nat. Commun.* **2** 379
- [199] Pfeleiderer C and Hackl R 2007 High-temperature superconductivity: schizophrenic electrons *Nature* **450** 492–3
- [200] Bonnell D *et al* 2012 Imaging physical phenomena with local probes: from electrons to photons *Rev. Mod. Phys.* **84** 1343–81
- [201] Huang P Y 2011 Grains and grain boundaries in single-layer graphene atomic patchwork quilts *Nature* **469** 389–92
- [202] Hanaguri T, Lupien C, Kohsaka Y, Lee D-H, Azuma M, Takano M, Takagi H and Davis J C 2004 A ‘checkerboard’ electronic crystal state in lightly hole-doped $\text{Ca}_{2-x}\text{Na}_x\text{CuO}_2\text{Cl}_2$ *Nature* **430** 1001–5
- [203] Gross L, Mohn F, Moll N, Liljeroth P and Meyer G 2009 The chemical structure of a molecule resolved by atomic force microscopy *Science* **325** 1110–4
- [204] Luan L *et al* 2010 Local measurement of the penetration depth in the pnictide superconductor $\text{Ba}(\text{Fe}_{0.95}\text{Co}_{0.05})_2\text{As}_2$ *Phys. Rev. B* **81** 100501
- [205] Auslaender O M *et al* 2009 Mechanics of individual isolated vortices in a cuprate superconductor *Nat. Phys.* **5** 35–9
- [206] Ricci A *et al* 2011 Nanoscale phase separation in the iron chalcogenide superconductor $\text{K}_{0.8}\text{Fe}_{1.6}\text{Se}_2$ as seen via scanning nanofocused x-ray diffraction *Phys. Rev. B* **84** 060511
- [207] Miao J, Ishikawa T, Robinson I K and Murnane M M 2015 Beyond crystallography: diffractive imaging using coherent x-ray light sources *Science* **348** 530
- [208] Keilmann F and Hillenbrand R 2004 Near-field microscopy by elastic light scattering from a tip *Phil. Trans. A* **362** 787–805
- [209] Ocelic N, Huber A and Hillenbrand R 2006 Pseudoheterodyne detection for background-free near-field spectroscopy *Appl. Phys. Lett.* **89** 101124
- [210] Hillenbrand R and Keilmann F 2000 Complex optical constants on a subwavelength scale *Phys. Rev. Lett.* **85** 3029–32
- [211] Govyadinov A A, Amenabar I, Huth F, Carney P S and Hillenbrand R 2013 Quantitative measurement of local infrared absorption and dielectric function with

- tip-enhanced near-field microscopy *J. Phys. Chem. Lett.* **4** 1526–31
- [212] Xu X G, Rang M, Craig I M and Raschke M B 2012 Pushing the sample-size limit of infrared vibrational nanospectroscopy: from monolayer toward single molecule sensitivity *J. Phys. Chem. Lett.* **3** 1836–41
- [213] Xu X G and Raschke M B 2013 Near-field infrared vibrational dynamics and tip-enhanced decoherence *Nano Lett.* **13** 1588–95
- [214] Hillenbrand R, Knoll B and Keilmann F 2001 Pure optical contrast in scattering-type scanning near-field microscopy *J. Microsc.* **202** 77–83
- [215] Bechtel H A, Muller E A, Olmon R L, Martin M C and Raschke M B 2014 Ultrabroadband infrared nanospectroscopic imaging *Proc. Natl Acad. Sci. USA* **111** 7191–6
- [216] Betzig E, Isaacson M and Lewis A 1987 Collection mode near-field scanning optical microscopy *Appl. Phys. Lett.* **51** 2088
- [217] Novotny L, Pohl D W and Hecht B 1995 Light confinement in scanning near-field optical microscopy *Ultramicroscopy* **61** 1–9
- [218] Veerman J A, Otter A M, Kuipers L and Van Hulst N F 1998 High definition aperture probes for near-field optical microscopy fabricated by focused ion beam milling *Appl. Phys. Lett.* **72** 3115–7
- [219] Hecht B, Sick B, Wild U P, Deckert V, Zenobi R, Martin O J F and Pohl D W 2000 Scanning near-field optical microscopy with aperture probes: fundamentals and applications *J. Chem. Phys.* **112** 7761
- [220] Frey H G, Keilmann F, Kriele A and Guckenberger R 2002 Enhancing the resolution of scanning near-field optical microscopy by a metal tip grown on an aperture probe *Appl. Phys. Lett.* **81** 5030
- [221] Biagioni P, Polli D, Labardi M, Pucci A, Ruggeri G, Cerullo G, Finazzi M and Duò L 2005 Unexpected polarization behavior at the aperture of hollow-pyramid near-field probes *Appl. Phys. Lett.* **87** 223112
- [222] Weber-Bargioni A *et al* 2011 Hyperspectral nanoscale imaging on dielectric substrates with coaxial optical antenna scan probes *Nano Lett.* **11** 1201–7
- [223] Mitrofanov O, Dominec F, Kužel P, Reno J L, Brener I, Chung U-C, Elissalde C, Maglione M and Mounaix P 2014 Near-field probing of mie resonances in single TiO₂ microspheres at terahertz frequencies *Opt. Express* **22** 23034
- [224] Courjon D and Bainier C 1999 Near field microscopy and near field optics *Rep. Prog. Phys.* **57** 989–1028
- [225] Bao W *et al* 2012 Mapping local charge recombination heterogeneity by multidimensional nanospectroscopic imaging *Science* **338** 1317–21
- [226] Soohoo R F 1962 A microwave magnetic microscope *J. Appl. Phys.* **33** 1276
- [227] Gao C and Xiang X-D 1998 Quantitative microwave near-field microscopy of dielectric properties *Rev. Sci. Instrum.* **69** 3846
- [228] Gao C, Duerwer F and Xiang X-D 1999 Quantitative microwave evanescent microscopy *Appl. Phys. Lett.* **75** 3005
- [229] Anlage S M, Talanov V V and Schwartz A R 2007 Principles of near-field microwave microscopy *Scanning Probe Microscopy: Electrical and Electromechanical Phenomena at the Nanoscale* ed S Kalinin and A Gruverman (Berlin: Springer)
- [230] Imtiaz A, Anlage S M, Barry J D and Melngailis J 2007 Nanometer-scale material contrast imaging with a near-field microwave microscope *Appl. Phys. Lett.* **90** 143106
- [231] Lai K, Peng H, Kundhikanjana W, Schoen D T, Xie C, Meister S, Cui Y, Kelly M A and Shen Z X 2009 Nanoscale electronic inhomogeneity in In₂Se₃ nanoribbons revealed by microwave impedance microscopy *Nano Lett.* **9** 1265–9
- [232] Lai K, Kundhikanjana W, Peng H, Cui Y, Kelly M A and Shen Z X 2009 Tapping mode microwave impedance microscopy *Rev. Sci. Instrum.* **80** 043707
- [233] Huber H P *et al* 2010 Calibrated nanoscale capacitance measurements using a scanning microwave microscope *Rev. Sci. Instrum.* **81** 113701
- [234] Kundhikanjana W, Lai K, Kelly M A and Shen Z X 2011 Cryogenic microwave imaging of metal–insulator transition in doped silicon *Rev. Sci. Instrum.* **82** 033705
- [235] Kundhikanjana W *et al* 2016 Direct imaging of dynamic glassy behavior in a strained manganite film *Phys. Rev. Lett.* **116** 019904
- [236] Hillenbrand R and Keilmann F 2002 Material-specific mapping of metal/semiconductor/dielectric nanosystems at 10 Nm resolution by backscattering near-field optical microscopy *Appl. Phys. Lett.* **80** 25–7
- [237] Lai K, Kundhikanjana W, Kelly M A, Shen Z X, Shabani J and Shayegan M 2011 Imaging of coulomb-driven quantum hall edge states *Phys. Rev. Lett.* **107** 176809
- [238] Murakami Y, Yoo J H, Shindo D, Atou T and Kikuchi M 2003 Magnetization distribution in the mixed-phase state of hole-doped manganites *Nature* **423** 965–8
- [239] Jin S, Tiefel T H, McCormack M, Fastnacht R A, Ramesh R and Chen L H 1994 Thousandfold change in resistivity in magnetoresistive La–Ca–Mn–O films *Science* **264** 413–5
- [240] Taubner T, Hillenbrand R and Keilmann F 2003 Performance of visible and mid-infrared scattering-type near-field optical microscopes *J. Microsc.* **210** 311–4
- [241] Chen H-T, Kersting R and Cho G C 2003 Terahertz imaging with nanometer resolution *Appl. Phys. Lett.* **83** 3009
- [242] Huth F, Govyadinov A, Amarie S, Nuansing W, Keilmann F and Hillenbrand R 2012 Nano-FTIR absorption spectroscopy of molecular fingerprints at 20 Nm spatial resolution *Nano Lett.* **12** 3973–8
- [243] Amarie S, Ganz T and Keilmann F 2009 Mid-infrared near-field spectroscopy *Opt. Express* **17** 21794–801
- [244] Keilmann F, Huber A J and Hillenbrand R 2009 Nanoscale conductivity contrast by scattering-type near-field optical microscopy in the visible, infrared and THz domains *J. Infrared Millim. Terahertz Waves* **30** 1255
- [245] Huber A, Ziegler A, Köck T and Hillenbrand R 2009 Infrared nanoscopy of strained semiconductors *Nat. Nanotechnol.* **4** 153–7
- [246] Keilmann F and Amarie S 2012 Mid-infrared frequency comb spanning an octave based on an Er fiber laser and difference-frequency generation *J. Infrared Millim. Terahertz Waves* **33** 479–84
- [247] Muller E A, Pollard B and Raschke M B 2015 Infrared chemical nano-imaging: accessing structure, coupling, and dynamics on molecular length scales *J. Phys. Chem. Lett.* **6** 1275–84
- [248] Qazilbash M M *et al* 2011 Nanoscale imaging of the electronic and structural transitions in vanadium dioxide *Phys. Rev. B* **83** 165108
- [249] Fei Z *et al* 2011 Infrared nanoscopy of dirac plasmons at the graphene-SiO₂ interface *Nano Lett.* **11** 4701–5
- [250] Yang H U, Hebestreit E, Josberger E E and Raschke M B 2013 A cryogenic scattering-type scanning near-field optical microscope *Rev. Sci. Instrum.* **84** 023701
- [251] Gerber J A, Berweger S, O’Callahan B T and Raschke M B 2014 Phase-resolved surface plasmon interferometry of graphene *Phys. Rev. Lett.* **113** 1–5
- [252] Stinson H T *et al* 2014 Infrared nanospectroscopy and imaging of collective superfluid excitations in anisotropic superconductors *Phys. Rev. B* **90** 1–10

- [253] Morin F J 1959 Oxides which show a metal-to-insulator transition at the neel temperature *Phys. Rev. Lett.* **3** 34–6
- [254] Goodenough J B 1971 Two components of the crystallographic transition in vanadium dioxide *J. Solid State Chem.* **3** 490–500
- [255] Pouget J P, Launois H, D’Haenens J P, Merenda P and Rice T M 1975 Electron localization induced by uniaxial stress in pure VO₂ *Phys. Rev. Lett.* **35** 873–5
- [256] Yajima T, Ninomiya Y, Nishimura T and Toriumi A 2015 Drastic change in electronic domain structures via strong elastic coupling in VO₂ films *Phys. Rev. B* **91** 205102
- [257] Laverock J, Kittiwatanakul S, Zakharov A A, Niu Y R, Chen B, Wolf S A, Lu J W and Smith K E 2014 Direct observation of decoupled structural and electronic transitions and an ambient pressure monocliniclike metallic phase of VO₂ *Phys. Rev. Lett.* **113** 216402
- [258] Kim J, Ko C, Frenzel A, Ramanathan S and Hoffman J E 2010 Nanoscale imaging and control of resistance switching in VO₂ at room temperature *Appl. Phys. Lett.* **96** 213106
- [259] Cao J *et al* 2009 Strain engineering and one-dimensional organization of metal–insulator domains in single-crystal vanadium dioxide beams *Nat. Nanotechnol.* **4** 732–7
- [260] Qazilbash M M *et al* 2009 Infrared spectroscopy and nano-imaging of the insulator-to-metal transition in vanadium dioxide *Phys. Rev. B* **79** 075107
- [261] Goldflam M D *et al* 2014 Voltage switching of a VO₂ memory metasurface using ionic gel *Appl. Phys. Lett.* **105**
- [262] Frenzel A, Qazilbash M M, Brehm M, Chae B-G, Kim B-J, Kim H-T, Balatsky A V, Keilmann F and Basov D N 2009 Inhomogeneous electronic state near the insulator-to-metal transition in the correlated oxide VO₂ *Phys. Rev. B* **80** 115115
- [263] Abate Y, Marvel R E, Ziegler J I, Gamage S, Javani M H, Stockman M I and Haglund R F 2015 Control of plasmonic nanoantennas by reversible metal–insulator transition *Sci. Rep.* **5** 13997
- [264] Wegkamp D *et al* 2014 Instantaneous band gap collapse in photoexcited monoclinic VO₂ due to photocarrier doping *Phys. Rev. Lett.* **113** 216401
- [265] Gray A X *et al* 2016 Correlation-driven insulator–metal transition in near-ideal vanadium dioxide films *Phys. Rev. Lett.* **116** 116403
- [266] Liu S, Phillabaum B, Carlson E W, Dahmen K A, Vidhyadhiraja N S, Qazilbash M M and Basov D N 2016 Random field driven spatial complexity at the mott transition in VO₂ *Phys. Rev. Lett.* **116** 036401
- [267] Louca D, Egami T, Brosha E, Röder H and Bishop A 1997 Local Jahn-Teller distortion in La_{1-x}Sr_xMnO₃ observed by pulsed neutron diffraction *Phys. Rev. B* **56** R8475–8
- [268] Millis A J, Shraiman B I and Mueller R 1996 Dynamic Jahn-Teller Effect and colossal magnetoresistance in La_{1-x}Sr_xMnO₃ *Phys. Rev. Lett.* **77** 175
- [269] Quijada M *et al* 1998 Optical conductivity of manganites: crossover from Jahn–Teller small polaron to coherent transport in the ferromagnetic state *Phys. Rev. B* **58** 16093
- [270] Millis A 1998 Lattice effects in magnetoresistive manganese perovskites *Nature* **392** 147–50
- [271] Röder H, Zang J and Bishop A 1996 Lattice effects in the colossal-magnetoresistance manganites *Phys. Rev. Lett.* **76** 1356
- [272] Loa I, Adler P, Grzechnik A, Syassen K, Schwarz U, Hanfland M, Rozenberg G K, Gorodetsky P and Pasternak M P 2001 Pressure-induced quenching of the Jahn–Teller distortion and insulator-to-metal transition in LaMnO₃ *Phys. Rev. Lett.* **87** 125501
- [273] Alonso J A, Martínez-Lope M J, Casais M T and Fernández-Díaz M T 2000 Evolution of the Jahn–Teller distortion of MnO₆ octahedra in RMnO₃ perovskites (R = Pr, Nd, Dy, Tb, Ho, Er, Y): a neutron diffraction study *Inorg. Chem.* **39** 917–23
- [274] Van Vleck J H 1937 The influence of dipole-dipole coupling on the specific heat and susceptibility of a paramagnetic salt *J. Chem. Phys.* **5** 320
- [275] Goodenough J B 1955 Theory of the role of covalence in the perovskite-type manganites [La,M(II)]MnO₃ *Phys. Rev.* **100** 564–73
- [276] Zhou J-S and Goodenough J 1998 Phonon-assisted double exchange in perovskite manganites *Phys. Rev. Lett.* **80** 2665–8
- [277] De Gennes P G 1960 Effects of double exchange in magnetic crystals *Phys. Rev.* **118** 141–54
- [278] Anderson P W and Hasegawa H 1955 Considerations on double exchange *Phys. Rev.* **100** 675–81
- [279] Kusters R M, Singleton J, Keen D A, McGreevy R and Hayes W 1989 Magnetoresistance measurements on the magnetic semiconductor Nd_{0.5}Pb_{0.5}MnO₃ *Physica B* **155** 362–5
- [280] von Helmolt R, Wecker J, Holzapfel B, Schultz L and Samwer K 1993 Giant negative magnetoresistance in perovskitelike La_{2/3}Ba_{1/3}MnO_x ferromagnetic films *Phys. Rev. Lett.* **71** 2331–3
- [281] Wollan E O and Koehler W C 1955 Neutron diffraction study of the magnetic properties of the series of perovskite-type compounds [(1 - x)La, xCa]MnO₃ *Phys. Rev.* **100** 545–63
- [282] Van Santen J H and Jonker G H 1950 Electrical conductivity of ferromagnetic compounds of manganese with perovskite structure *Physica* **16** 599–600
- [283] Jonker G H and Van Santen J H 1950 Ferromagnetic compounds of manganese with perovskite structure *Physica* **16** 337–49
- [284] Raquet B, Anane A, Wirth S, Xiong P and von Molnar S 2000 Noise probe of the dynamic phase separation in La_{2/3}Ca_{1/3}MnO₃ *Phys. Rev. Lett.* **84** 4486
- [285] Kiryukhin V 1997 An x-ray-induced insulator–metal transition in a magnetoresistive manganite *Nature* **386** 813
- [286] Soh Y A, Evans P G, Cai Z, Lai B, Kim C Y, Aeppli G, Mathur N D, Blamire M G and Isaacs E D 2002 Local mapping of strain at grain boundaries in colossal magnetoresistive films using x-ray microdiffraction *J. Appl. Phys.* **91** 7742–4
- [287] Kuhns P, Hoch M, Moulton W, Reyes A, Wu J and Leighton C 2003 Magnetic phase separation in La_{1-x}Sr_xCoO₃ by Co59 nuclear magnetic resonance *Phys. Rev. Lett.* **91** 127202
- [288] Chechersky V, Nath A and Michel C 2000 Emission Mössbauer study of the electronic phases in La_{0.7}Ca_{0.3}MnO₃ *Phys. Rev. B* **62** 5316–9
- [289] Renner C, Aeppli G, Kim B-G, Soh Y-A and Cheong S-W 2002 Atomic-scale images of charge ordering in a mixed-valence manganite *Nature* **416** 518–21
- [290] Fäth M 1999 Spatially inhomogeneous metal–insulator transition in doped manganites *Science* **285** 1540–2
- [291] Becker T, Streng C, Luo Y, Moshnyaga V, Damaschke B, Shannon N and Samwer K 2002 Intrinsic inhomogeneities in manganite thin films investigated with scanning tunneling spectroscopy *Phys. Rev. Lett.* **89** 237203
- [292] Ahn K H, Seman T F, Lookman T and Bishop A R 2013 Role of complex energy landscapes and strains in multiscale inhomogeneities in perovskite manganites *Phys. Rev. B* **88** 144415
- [293] Aen C, Liang S and Dagotto E 2012 Complex state found in the colossal magnetoresistance regime of models for manganites *Phys. Rev. B* **85** 174418

- [294] Fontcuberta J, Martínez B, Seffar A, Piñol S, García-Muñoz J and Obradors X 1996 Colossal magnetoresistance of ferromagnetic manganites: structural tuning and mechanisms *Phys. Rev. Lett.* **76** 1122–5
- [295] Singh-Bhalla G, Biswas A and Hebard A F 2009 Tunneling magnetoresistance in phase-separated manganite nanobridges *Phys. Rev. B* **80** 144410
- [296] Hattori A N, Fujiwara Y, Fujiwara K, Nguyen A T V, Nakamura T, Ichimiya M, Ashida M and Tanaka H 2015 Identification of giant mott phase transition of single electric nanodomain in manganite nanowall wire *Nano Lett.* **15** 4322–8
- [297] Du K *et al* 2015 Visualization of a ferromagnetic metallic edge state in manganite strips *Nat. Commun.* **6** 6179
- [298] Ma E Y *et al* 2015 Mobile metallic domain walls in an all-in-all-out magnetic insulator *Science* **350** 538–41
- [299] Moon S J *et al* 2008 Dimensionality-controlled insulator–metal transition and correlated metallic state in $\text{Sr}_{n+1}\text{Ir}_n\text{O}_{3n+1}$ ($n = 1, 2$ and ∞) *Phys. Rev. Lett.* **101** 226402
- [300] Wan X, Turner A M, Vishwanath A and Savrasov S Y 2011 Topological semimetal and fermi-arc surface states in the electronic structure of pyrochlore iridates *Phys. Rev. B* **83** 205101
- [301] Tomiyasu K *et al* 2012 Emergence of magnetic long-range order in frustrated pyrochlore $\text{Nd}_2\text{Ir}_2\text{O}_7$ with metal–insulator transition *J. Phys. Soc. Japan* **81** 034709
- [302] Ueda K, Fujioka J, Takahashi Y, Suzuki T, Ishiwata S, Taguchi Y and Tokura Y 2012 Variation of charge dynamics in the course of metal–insulator transition for pyrochlore-type $\text{Nd}_2\text{Ir}_2\text{O}_7$ *Phys. Rev. Lett.* **109** 136402
- [303] Arima T H 2013 Time-reversal symmetry breaking and consequent physical responses induced by all-in-all-out type magnetic order on the pyrochlore lattice *J. Phys. Soc. Japan* **82** 013705–1
- [304] Matsuhira K, Tokunaga M, Wakeshima M, Hinatsu Y and Takagi S 2013 Giant magnetoresistance effect in the metal–insulator transition of pyrochlore oxide $\text{Nd}_2\text{Ir}_2\text{O}_7$ *J. Phys. Soc. Japan* **82** 023706
- [305] Sleight A W, Gillson J L, Weiher J F and Bindloss W 1974 Semiconductor-metal transition in novel $\text{Cd}_2\text{Os}_2\text{O}_7$ *Solid State Commun.* **14** 357–9
- [306] Mandrus D *et al* 2001 Continuous metal–insulator transition in the pyrochlore $\text{Cd}_2\text{Os}_2\text{O}_7$ *Phys. Rev. B* **63** 195104
- [307] Jin R, He J, McCall S, Alexander C S, Drymiotis F and Mandrus D 2001 Superconductivity in the correlated pyrochlore $\text{Cd}_2\text{Re}_2\text{O}_7$ *Phys. Rev. B* **64** 180503
- [308] Sohn C H *et al* 2015 Optical spectroscopic studies of the metal–insulator transition driven by all-in–all-out magnetic ordering in 5d pyrochlore $\text{Cd}_2\text{Os}_2\text{O}_7$ *Phys. Rev. Lett.* **115** 266402
- [309] Hiroi Z, Yamaura J, Hirose T, Nagashima I and Okamoto Y 2015 Lifshitz metal–insulator transition induced by the all-in/all-out magnetic order in the pyrochlore oxide $\text{Cd}_2\text{Os}_2\text{O}_7$ *APL Mater.* **3** 041501
- [310] Yamaura J *et al* 2012 Tetrahedral magnetic order and the metal–insulator transition in the pyrochlore lattice of $\text{Cd}_2\text{Os}_2\text{O}_7$ *Phys. Rev. Lett.* **108** 247205
- [311] Shinaoka H, Miyake T and Ishibashi S 2012 Noncollinear magnetism and spin–orbit coupling in 5d pyrochlore oxide $\text{Cd}_2\text{Os}_2\text{O}_7$ *Phys. Rev. Lett.* **108** 247204
- [312] Chern G W and Batista C D 2011 Spin superstructure and noncoplanar ordering in metallic pyrochlore magnets with degenerate orbitals *Phys. Rev. Lett.* **107** 186403
- [313] Tardif S, Takeshita S, Ohsumi H, Yamaura J, Okuyama D, Hiroi Z, Takata M and Arima T 2015 All-in–all-out magnetic domains: x-ray diffraction imaging and magnetic field control *Phys. Rev. Lett.* **114** 147205
- [314] Fradkin E and Kivelson S A 2012 High-temperature superconductivity: ineluctable complexity *Nat. Phys.* **8** 864–6
- [315] Campi G *et al* 2013 Inhomogeneity of charge-density-wave order and quenched disorder in a high- T_c superconductor *Nature* **525** 359
- [316] Allan M, Chuang T-M, Masee F and Xie Y 2013 Anisotropic impurity states, quasiparticle scattering and nematic transport in underdoped Ca $(\text{Fe}_{1-x}\text{Co}_x)_2\text{As}_2$ *Nat. Phys.* **9** 220–4
- [317] Chen F *et al* 2011 Electronic identification of the parental phases and mesoscopic phase separation of $\text{K}_x\text{Fe}_{2-y}\text{Se}_2$ superconductors *Phys. Rev. X* **1** 021020
- [318] Bednorz J G and Müller K A 1986 Possible high T_c superconductivity in the Ba–La–Cu–O System *Z. Phys. B* **64** 189–93
- [319] Wu D *et al* 2010 Optical investigations of the normal and superconducting states reveal two electronic subsystems in iron pnictides *Phys. Rev.* **81** 100512
- [320] Moon S J, Schafgans A A, Tanatar M A, Prozorov R, Thaler A, Canfield P C, Sefat A S, Mandrus D and Basov D N 2013 Interlayer coherence and superconducting condensate in the c -axis response of optimally doped $\text{Ba}(\text{Fe}_{1-x}\text{Co}_x)_2\text{As}_2$ high- T_c superconductor using infrared spectroscopy *Phys. Rev. Lett.* **110** 097003
- [321] Charnukha A *et al* 2012 Optical conductivity of superconducting $\text{Rb}_2\text{Fe}_4\text{Se}_5$ single crystals *Phys. Rev. B* **85** 100504
- [322] Li G, Hu W Z, Dong J, Li Z, Zheng P, Chen G F, Luo J L and Wang N L 2008 Probing the superconducting energy gap from infrared spectroscopy on a $\text{Ba}_{0.6}\text{K}_{0.4}\text{Fe}_2\text{As}_2$ single crystal with $T_c = 37$ K *Phys. Rev. Lett.* **101** 107004
- [323] Charnukha A 2014 Optical conductivity of iron-based superconductors *J. Phys.* **26** 253203
- [324] Lucarelli A, Dusza A, Pfuner F, Lerch P, Analytis J G, Chu J H, Fisher I R and Degiorgi L 2010 Charge dynamics of co-doped BaFe_2As_2 *New J. Phys.* **12** 073036
- [325] Nakajima M *et al* 2010 Evolution of the optical spectrum with doping in $\text{Ba}(\text{Fe}_{1-x}\text{Co}_x)_2\text{As}_2$ *Phys. Rev. B* **81** 104528
- [326] van Heumen E, Huang Y, de Jong S, Kuzmenko A B, Golden M S and van der Marel D 2010 Optical properties of $\text{BaFe}_{2-x}\text{Co}_x\text{As}_2$ *Europhys. Lett.* **90** 37005
- [327] Kim K W, Rössle M, Dubroka A, Malik V K, Wolf T and Bernhard C 2010 Evidence for multiple superconducting gaps in optimally doped $\text{BaFe}_{1.87}\text{Co}_{0.13}\text{As}_2$ from infrared spectroscopy *Phys. Rev. B* **81** 214508
- [328] Wu D, Chanda G, Jeevan H S, Gegenwart P and Dressel M 2011 Optical investigations of chemically pressurized $\text{EuFe}_2(\text{As}_{1-x}\text{P}_x)_2$: an S-wave superconductor with strong interband interactions *Phys. Rev. B* **83** 100503
- [329] Wang N L, Hu W Z, Chen Z G, Yuan R H, Li G, Chen G F and Xiang T 2012 High energy pseudogap and its evolution with doping in Fe-based superconductors as revealed by optical spectroscopy *J. Phys.* **24** 294202
- [330] Schafgans A A *et al* 2012 Electronic correlations and unconventional spectral weight transfer in the high-temperature pnictide $\text{BaFe}_{2-x}\text{Co}_x\text{As}_2$ superconductor using infrared spectroscopy *Phys. Rev. Lett.* **108** 147002
- [331] Moon S J *et al* 2012 Infrared measurement of the pseudogap of P-Doped and Co-doped high-temperature BaFe_2As_2 superconductors *Phys. Rev. Lett.* **109** 027006
- [332] Moon S J *et al* 2014 Infrared pseudogap in cuprate and pnictide high-temperature superconductors *Phys. Rev. B* **90** 014503
- [333] Chen Z G *et al* 2011 Infrared spectrum and its implications for the electronic structure of the semiconducting iron selenide $\text{K}_{0.83}\text{Fe}_{1.53}\text{Se}_2$ *Phys. Rev.* **83** 220507

- [334] Basov D N, Dabrowski B and Timusk T 1998 Infrared probe of transition from superconductor to nonmetal in $\text{YBa}_2(\text{Cu}_{1-x}\text{Zn}_x)_4\text{O}_8$ *Phys. Rev. Lett.* **81** 2132–5
- [335] Dumm M, Komiya S, Ando Y and Basov D 2003 Anisotropic electromagnetic response of lightly doped $\text{La}_{2-x}\text{Sr}_x\text{CuO}_4$ within the CuO_2 planes *Phys. Rev. Lett.* **91** 077004
- [336] Tajima S, Wang N L, Ichikawa N, Eisaki H, Uchida S, Kitano H, Hanaguri T and Maeda A 1999 In-plane charge dynamics in $\text{La}_{1.6-x}\text{Nd}_{0.4}\text{Sr}_x\text{CuO}_4$: absence of a charge gap in the spin/charge ordered state *Europhys. Lett.* **47** 715–21
- [337] Homes C C, Tranquada J M, Li Q, Moodenbaugh A R and Buttrey D J 2003 Mid-infrared conductivity from mid-gap states associated with charge stripes *Phys. Rev. B* **67** 184516
- [338] Homes C C, Hücker M, Li Q, Xu Z J, Wen J S, Gu G D and Tranquada J M 2012 Determination of the optical properties of $\text{La}_{2-x}\text{Ba}_x\text{CuO}_4$ for several dopings, including the anomalous $x = 1/8$ phase *Phys. Rev. B* **85** 134510
- [339] Lee Y S, Segawa K, Ando Y and Basov D N 2004 Quasiparticle dynamics and in-plane anisotropy in $\text{YBa}_2\text{Cu}_3\text{O}_y$ near the onset of superconductivity *Phys. Rev. B* **70** 014518
- [340] Orenstein J 2003 Optical conductivity of a superfluid density wave *Physica C* **390** 243–8
- [341] Ghiringhelli G *et al* 2012 Long-range incommensurate charge fluctuations in $(\text{Y,Nd})\text{Ba}_2\text{Cu}_3\text{O}_{6+x}$ *Science* **337** 821–5
- [342] Blanco-Canosa S 2013 Momentum-dependent charge correlations in $\text{YBa}_2\text{Cu}_3\text{O}_{6+d}$ superconductors probed by resonant x-ray scattering: evidence for three competing phases *Phys. Rev. Lett.* **110** 187001
- [343] Blackburn E *et al* 2013 X-ray diffraction observations of a charge-density-wave order in superconducting ortho-II $\text{YBa}_2\text{Cu}_3\text{O}_{6.54}$ single crystals in zero magnetic field *Phys. Rev. Lett.* **110** 137004
- [344] Walmsley P *et al* 2013 Quasiparticle mass enhancement close to the quantum critical point in $\text{BaFe}_2(\text{As}_{1-x}\text{P}_x)_2$ *Phys. Rev. Lett.* **110** 257002
- [345] Nakajima M *et al* 2011 Unprecedented anisotropic metallic state in undoped iron arsenide BaFe_2As_2 revealed by optical spectroscopy *Proc. Natl Acad. Sci. USA* **108** 12238–42
- [346] Nakajima M *et al* 2012 Effect of Co doping on the in-plane anisotropy in the optical spectrum of underdoped $\text{Ba}(\text{Fe}_{1-x}\text{Co}_x)_2\text{As}_2$ *Phys. Rev. Lett.* **109** 217003
- [347] Mirri C, Dusza A, Bastelberger S, Chinotti M, Degiorgi L, Chu J H, Kuo H H and Fisher I R 2015 Origin of the resistive anisotropy in the electronic nematic phase of BaFe_2As_2 revealed by optical spectroscopy *Phys. Rev. Lett.* **115** 107001
- [348] Dusza A, Lucarelli A, Pfuner F, Chu J-H, Fisher I R and Degiorgi L 2011 Anisotropic charge dynamics in detwinned $\text{Ba}(\text{Fe}_{1-x}\text{Co}_x)_2\text{As}_2$ *Europhys. Lett.* **93** 37002
- [349] Kalisky B, Kirtley J R, Analytis J G, Chu J H, Vailionis A, Fisher I R and Moler K A 2010 Stripes of increased diamagnetic susceptibility in underdoped superconducting $\text{Ba}(\text{Fe}_{1-x}\text{Co}_x)_2\text{As}_2$ single crystals: evidence for an enhanced superfluid density at twin boundaries *Phys. Rev. B* **81** 184513
- [350] Charnukha A *et al* 2012 Nanoscale layering of antiferromagnetic and superconducting phases in $\text{Rb}_2\text{Fe}_4\text{Se}_5$ single crystals *Phys. Rev. Lett.* **109** 017003
- [351] Jiang H M, Chen W Q, Yao Z J and Zhang F C 2012 Superconducting proximity effect on the block antiferromagnetism in $\text{K}_x\text{Fe}_{2-x}\text{Se}_2$ *Phys. Rev. B* **85** 104506
- [352] Ge J, Liu Z-L, Liu C, Gao C, Qian D, Xue Q, Liu Y and Jia J-F 2014 Superconductivity above 100 K in single-layer FeSe films on doped SrTiO_3 *Nat. Mater.* **14** 285–9
- [353] He S *et al* 2013 Phase diagram and electronic indication of high-temperature superconductivity at 65 K in single-layer FeSe films *Nat. Mater.* **12** 605–10
- [354] Wang Z, Cai Y, Wang Z W, Ma C, Chen Z, Yang H X, Tian H F and Li J Q 2015 Archimedean solidlike superconducting framework in phase-separated $\text{K}_{0.8}\text{Fe}_{1.6+x}\text{Se}_2$ ($0 \leq x \leq 0.15$) *Phys. Rev. B* **91** 064513
- [355] Liu Y, Xing Q, Straszheim W E, Marshman J, Pedersen P and Lograsso A 2016 *In situ* observation of phase separation and hierarchical microstructure of $\text{K}_x\text{Fe}_{2-y}\text{Se}_2$ single crystals *Phys. Rev. B* **93** 064509
- [356] Kaindl R A and Averitt R D 2001 *Time-Resolved THz Studies of Carrier Dynamics in Semiconductors, Superconductors, and Strongly-Correlated Electron Materials* 2nd edn (Berkeley, CA: University of California Press)
- [357] Yonemitsu K and Nasu K 2006 Theory of photoinduced phase transitions *J. Phys. Soc. Japan* **75** 011008
- [358] Liu M K *et al* 2011 Photoinduced phase transitions by time-resolved far-infrared spectroscopy in V_2O_3 *Phys. Rev. Lett.* **107** 66403
- [359] de Jong S *et al* 2013 Speed limit of the insulator–metal transition in magnetite *Nat. Mater.* **12** 882–6
- [360] Abreu E *et al* 2015 Dynamic conductivity scaling in photoexcited V_2O_3 thin films *Phys. Rev. B* **92** 085130
- [361] Verwey E J W 1939 Electronic conduction of magnetite (Fe_3O_4) and its transition point at low temperatures *Nature* **144** 327–8
- [362] Senn M S S, Wright J P P and Attfield J P P 2011 Charge order and three-site distortions in the Verwey structure of magnetite *Nature* **481** 173–6
- [363] Först M, Manzoni C, Kaiser S, Tomioka Y, Tokura Y, Merlin R and Cavalleri A 2011 Nonlinear phononics as an ultrafast route to lattice control *Nat. Phys.* **7** 854–6
- [364] Siders C W and Cavalleri A 2003 Creating transient crystal structures with light *Science* **300** 591
- [365] Ehrke H *et al* 2011 Photoinduced melting of antiferromagnetic order in $\text{La}_{0.5}\text{Sr}_{1.5}\text{MnO}_4$ measured using ultrafast resonant soft x-ray diffraction *Phys. Rev. Lett.* **106** 217401
- [366] Rini M *et al* 2008 Optical switching in VO_2 films by below-gap excitation *Appl. Phys. Lett.* **92** 181904
- [367] Miyano K, Tanaka T, Tomioka Y and Tokura Y 1997 Photoinduced insulator-to-metal transition in a perovskite manganite *Phys. Rev. Lett.* **78** 4257–60
- [368] Collet E *et al* 2003 Laser-induced ferroelectric structural order in an organic charge-transfer crystal *Science* **300** 612–5
- [369] Guo H, Noh J H, Dong S, Rack P D, Gai Z, Xu X, Dagotto E, Shen J and Ward T Z 2013 Electrophoretic-like gating used to control metal–insulator transitions in electronically phase separated manganite wires *Nano Lett.* **13** 3749–54
- [370] Li M, Graf T, Schladt T D, Jiang X and Parkin S S P 2012 Role of percolation in the conductance of electrolyte-gated SrTiO_3 *Phys. Rev. Lett.* **109** 196803
- [371] Lourembam J, Wu J, Ding J, Lin W and Wu T 2014 Electric field tuning of phase separation in manganite thin films *Phys. Rev. B* **89** 014425
- [372] Ren Y, Yuan H, Wu X, Chen Z, Iwasa Y, Cui Y, Hwang H Y and Lai K 2015 Direct imaging of nanoscale conductance evolution in ion-gel-gated oxide transistors *Nano Lett.* **15** 4730–6



Mengkun Liu received the PhD degree in physics from Boston University, Boston, MA, USA, in 2012. Following this, he was a Post-Doctoral researcher at UC San Diego, San Diego, CA, USA. His postdoctoral work focused on infrared near-field imaging and spectroscopy of strongly correlated electron materials. In 2015, he joined Stony Brook University, Stony Brook, NY, USA, as an assistant Professor with the Department of Physics and Astronomy. His research interests cover nanoscale and ultrafast electromagnetic responses of strongly correlated electron materials, 2D materials and meta-materials, which span from the near-infrared through the terahertz frequencies.



Dmitri N Basov is the Higgins Professor of Physics at Columbia University. His research interests include novel physics of quantum materials that he investigates using novel optical techniques developed in his group. He received his PhD from the Academy of Sciences of the USSR in 1991. He has held a postdoctoral appointment at McMaster University and an assistant physicist position at Brookhaven National Laboratory. Between 1997 and 2016 he was on the faculty at the University of California San Diego before accepting a position at Columbia.